The Astrophysical Journal Supplement Series, 275:1 (29pp), 2024 November https://doi.org/10.3847/1538-4365/ad71d6

X-Ray Emission of Nearby Low-mass and Sunlike Stars with Directly Imageable Habitable Zones

Breanna A. Binder[1], Sarah Peacock[2,3], Edward W. Schwieterman[4,5], Margaret C. Turnbull[6], Azariel Y. Virgen[1], Stephen R. Kane[4], Alison Farrish[3], and Katherine Garcia-Sage[7]
[1] Department of Physics and Astronomy, California State Polytechnic University, Pomona, CA 91768, USA; babinder@cpp.edu
[2] University of Maryland, Baltimore County, Baltimore, MD 21250, USA
[3] NASA Goddard Space Flight Center, Greenbelt, MD 20771, USA
[4] Department of Earth and Planetary Sciences, University of California, Riverside, CA 92521, USA
[5] Blue Marble Space Institute of Science, Seattle, WA 98185, USA
[6] SETI Institute, Carl Sagan Center for the Study of Life in the Universe; Off-site: Madison, WI 53713, USA
[7] Heliophysics Division, NASA Goddard Space Flight Center, Greenbelt, MD 20771, USA
Received 2024 June 10; revised 2024 July 25; accepted 2024 July 30; published 2024 October 15

Abstract

Stellar X-ray and UV radiation can significantly affect the survival, composition, and long-term evolution of the atmospheres of planets in or near their host star's habitable zone (HZ). Especially interesting are planetary systems in the solar neighborhood that may host temperate and potentially habitable surface conditions, which may be analyzed by future ground- and space-based direct-imaging surveys for signatures of habitability and life. To advance our understanding of the radiation environment in these systems, we leverage ∼3 Ms of XMM-Newton and Chandra observations in order to measure three fundamental stellar properties at X-ray energies for 57 nearby FGKM stellar systems: the shape of the stellar X-ray spectrum, the luminosity, and the timescales over which the stars vary (e.g., due to flares). These systems possess HZs that will be directly imageable to next-generation telescopes such as the Habitable Worlds Observatory and ground-based Extremely Large Telescopes. We identify 29 stellar systems with L_X/L_{bol} ratios similar to (or less than) that of the Sun; any potential planets in the HZs of these stars therefore reside in present-day X-ray radiation environments similar to (or less hostile than) modern Earth, though a broader set of these targets could host habitable planets. An additional 19 stellar systems have been observed with the Swift X-ray Telescope; in total, only ∼30% of potential direct imaging target stars has been observed with XMM-Newton, Chandra, or Swift. The data products from this work (X-ray light curves and spectra) are available via a public Zenodo repository (doi:10.5281/zenodo.11490574).

Unified Astronomy Thesaurus concepts: Planet hosting stars (1242); Stellar x-ray flares (1637); F dwarf stars (516); G dwarf stars (556); K dwarf stars (876); Dwarf planets (419); Habitable planets (695)

Materials only available in the online version of record: animation, figure set, machine-readable tables

1. Introduction

In the coming decades, ground- and space-based direct imaging will afford the best potential for detecting and spectrally characterizing terrestrial planets in the habitable zones (HZs) of our nearest neighbors (R. K. Kopparapu et al. 2018; S. R. Kane et al. 2018; Z. Li et al. 2021; M. C. Turnbull et al. 2021; T. Currie et al. 2023). While the James Webb Space Telescope (JWST) has and will continue to characterize some rocky exoplanets (e.g., T. P. Greene et al. 2023; A. P. Lincowski et al. 2023; J. Lustig-Yaeger et al. 2023; S. E. Moran et al. 2023; S. Zieba et al. 2023), its ability to spectrally examine temperate terrestrial—and therefore potentially habitable—exoplanets is limited primarily to target systems with transiting planets and late-M dwarf host stars. This is due to the lack of coronagraphic instrumentation on JWST to image rocky planets around more massive, Sunlike stars, and because the characterization of terrestrial planets through transit observations is most favorable for M dwarf hosts, which have a combination of favorable transit probabilities, planet-to-star size ratios, and planet–star separations that allow for the probing of low atmospheric altitudes when accounting for the effects of refraction (A. García Muñoz et al. 2012; Y. Bétrémieux & L. Kaltenegger 2013, 2014). Moreover, some key candidate biosignature molecules like O_2 cannot be detected directly at Earthlike abundances with JWST via transit spectroscopy even for the most favorable targets (e.g., J. Lustig-Yaeger et al. 2019; D. Pidhorodetska et al. 2020; V. S. Meadows et al. 2023), but could be more easily detected by reflected light observations of planets in nearby systems (The LUVOIR Team 2019; B. S. Gaudi et al. 2020).

The occurrence rates derived from Kepler indicate that terrestrial planets are likely present within the HZs of a large fraction of nearby stars (e.g., S. R. Kane et al. 2014; C. J. Burke et al. 2015; B. J. Fulton et al. 2017; M. Kunimoto & J. M. Matthews 2020; S. Bryson et al. 2021; A. Dattilo et al. 2023). The Astro2020 Decadal Survey has identified the discovery and characterization of these worlds as the highest priority for NASA's investments (National Academies of Sciences, Engineering, & Medicine 2023), and the Habitable Worlds Observatory (HWO)[8] will build on the LUVOIR and Habitable Exoplanets Observatory concepts (The LUVOIR Team 2019; B. S. Gaudi et al. 2020) to realize this goal. Due to detection biases, the vast majority of nearby temperate rocky

[8] https://habitableworldsobservatory.org/home

planets amenable for direct imaging have not yet been discovered, but will be revealed by HWO in its survey phase (e.g., The LUVOIR Team 2019; B. S. Gaudi et al. 2020), precursor science with extreme precision radial velocity measurements (J. Crass et al. 2021; R. Morgan et al. 2021), or direct imaging with upcoming 30 m class telescopes (Y. Fujii et al. 2018; T. Currie et al. 2023).

A detailed understanding of the target stars themselves is a strong prerequisite for maximizing the science yield of exoplanet imaging missions, including extracting the statistical features of the overall planet population (e.g., V. Van Eylen et al. 2014) as well as characterizing the climates, atmospheric composition and stability (A. J. Louca et al. 2023; J. L. Linsky & S. Redfield 2024), and potential biosignatures of individual planets (S. Rugheimer et al. 2015; E. W. Schwieterman et al. 2018). Evaluating planetary habitability, specifically, must consider myriad factors beyond circumstellar location including the planet's bulk composition (N. R. Hinkel & C. T. Unterborn 2018; N. Marounina & L. A. Rogers 2020; C. T. Unterborn et al. 2023) and stellar X-ray and extreme ultraviolet (XUV; 1–912 Å; corresponding to an energy range of 0.01–12 keV) emission (R. Luger & R. Barnes 2015; K. France et al. 2016; K. Garcia-Sage et al. 2017; T. Richey-Yowell et al. 2019). Planets orbiting in or near their star's HZ can experience high levels of XUV radiation, which directly influences atmospheric survival, composition, and long-term evolution (S. Peacock et al. 2020; C. P. Johnstone et al. 2021). In some cases, planetary atmospheres and surface volatiles can be entirely driven away by XUV irradiation (e.g., J. Sanz-Forcada et al. 2011; R. Luger & R. Barnes 2015; E. F. Fromont et al. 2024). Further, the atmospheric states of planets orbiting M dwarf stars may be profoundly different than for those orbiting Sunlike FGK stars due their to extended superluminous pre-main-sequence phase (I. Baraffe et al. 2015) during which XUV radiation could ablate away planetary atmospheres or lead to atmospheric oxidation via massive H escape (R. Luger & R. Barnes 2015; K. Garcia-Sage et al. 2017; J. Krissansen-Totton & J. J. Fortney 2022). Outgassing could replenish these atmospheres (S. R. Kane et al. 2020a; E. S. Kite & M. N. Barnett 2020; M. R. Swain et al. 2021; C. T. Unterborn et al. 2022), though the retention and photochemistry of the atmosphere would continue to be controlled by the host star spectrum and activity (K. France et al. 2016; R. M. Roettenbacher & S. R. Kane 2017; R. O. P. Loyd et al. 2018a, 2018b; K. France et al. 2020; L. N. R. do Amaral et al. 2022).

While X-ray detections have been made for some HWO target stars (C. K. Harada et al. 2024) and more detailed studies of the X-ray properties of low-mass nearby stars have been performed (R. O. P. Loyd et al. 2018b; K. France et al. 2020; A. Brown et al. 2023), no comprehensive and uniform X-ray analysis of potential direct imaging target stars has yet been done. In this paper, we present a comprehensive analysis of archival X-ray observations for all FGKM stellar systems with HZs that will be directly imageable with upcoming telescopes such as HWO and ground-based Extremely Large Telescopes (ELTs). A follow-up paper yielding panchromatic XUV–IR spectra (including modeled EUV wavelengths) for each one of these systems is forthcoming (S. Peacock et al. 2024, in preparation). We describe our sample and the archival data in Sections 2 and 3. Our analysis procedure is detailed in Section 4. We extract light curves for stars detected at high significance and identify periods of count rate variability (such as flaring events or epochs of elevated count rates). We then extract X-ray spectra for stars, separating variable- from nonvariable epochs, and fit the resulting spectra with one-, two-, or three-component thermal plasma models. Finally, the average best-fit spectral models are used to convert observed count rates (or count rate upper limits, in the case of non-X-ray-detected stars) to luminosities. In Section 5, we discuss the evolution of the L_X/L_{bol} ratio with effective temperature and stellar age, and present extensive Appendices (A and B) describing the X-ray observations and a summary of the known stellar physical parameters and exoplanet systems from the literature for each stellar system in our sample.

2. The Sample

To identify the highest-priority targets for "deep dive" investigations of nearby stars and their planetary systems, we have used the predicted imaging and spectroscopy capability of (1) NASA's next-generation space-based Great Observatories such as HWO, and (2) ground-based ELTs. To first order, the performance of these facilities is described in terms of two specifications: (1) the inner working angle (IWA)—the smallest planet–star angular separation that can be imaged (expressed in milliarcseconds); and (2) the minimum planet to star flux ratio (or fractional planet brightness, FPB)—where starlight suppression technology and postprocessing algorithms can separate the planet signal from stellar photons and systematic noise. Intriguingly (and somewhat vexingly), for HZ planets, the IWA requirement favors stars that are more luminous and therefore have wider HZs, while the limiting flux ratio favors target stars that are less luminous and therefore outshine their HZ planets by a smaller factor (M. C. Turnbull et al. 2012). A third specification, planet limiting magnitude (V_{lim}), determines which of these targets planets would be bright enough to obtain spectra in a reasonable amount of observing time—and this requirement simply favors the nearest stars.

To form our preliminary target list, for space-based missions, we chose stars for which the HZ (0.95–1.7 au scaled by $\sqrt{L_{bol}}$) falls at least partially outside an IWA of 58 mas, and for which Earth-sized planets of albedo ∼0.3 would be brighter than $V_{lim} < 30$, with an FPB $>4 \times 10^{-11}$. For ground-based observatories, we examined the 25 stars within 10 pc having the most favorable FPB whose HZs are at least partially visible outside an IWA of ∼30 mas, consistent with the literature (S. P. Quanz et al. 2015; B. R. Brandl et al. 2018). This results in a well-defined list of 175 target stars whose HZs fall at least partially within the detection space of upcoming exoplanet direct imaging observatories. We compared our target list with the potential target stars for HWO (E. Mamajek & K. Stapelfeldt 2024), who used slightly different cutoff requirements for V_{lim}, FPB, and IWA. Our list contains more M dwarfs (more favorable targets for ELTs) while the E. Mamajek & K. Stapelfeldt (2024) list includes more F stars (more favorable for space-based observations). E. Mamajek & K. Stapelfeldt (2024) also excluded stars in close binaries or higher-order multiple systems, while we produce a more inclusive X-ray catalog of nearby stars, assuming technical challenges posed by binaries may eventually be surmounted. There are 229 unique stars when combining the two lists, which we summarize in Table 1.

Using this input list of 229 viable targets for direct imaging campaigns, we searched the archives of the XMM-Newton

Table 1
Potential Target Stars for Future HZ Imaging Surveys

HD ID	Common Name	Distance (pc)	Spectral Type	From This Work?	Potential HWO Target[a]
166	V439 And	13.77	G8V	✓	✓
693	6 Cet	18.89	F8V		✓
739	θ Scl	21.72	F5V		✓
1326	GX And	3.57	M1.5V	✓	
1581	ζ Tuc	8.61	F9.5V	✓	✓

Note.
[a] From E. Mamajek & K. Stapelfeldt (2024).

(This table is available in its entirety in machine-readable form in the online article.)

Observatory and the Chandra X-ray Observatory for publicly available data. Many M stars (and some K stars) in this initial target list were previously studied as part of the Measurements of the Ultraviolet Spectral Characteristics of Low-mass Exoplanetary systems (MUSCLES) and Mega-MUSCLES Hubble Space Telescope Treasury programs, which characterized the X-ray/UV emission from K and M exoplanet host stars. We incorporate these results, presented in A. Brown et al. (2023), into our work here (see Section 5). We retrieve 192 XMM-Newton and Chandra observations for 57 stellar systems containing Sunlike and low-mass stars from the X-ray archives, amounting to ∼3 Ms of observing time (not including the MUSCLES/Mega-MUSCLES observations). An additional 19 stellar systems have been observed by Swift. Figure 1 shows a map of the 3D spatial distribution of these nearby stars and indicates which stars have X-ray observations available.

There are three M dwarfs highlighted in E. Mamajek & K. Stapelfeldt (2024) as strong potential HWO targets (Lacaille 8760, Lacaille 9352, and Lalande 21185). Both Lacaille 8760 and Lacaille 9352 were observed by Swift and are included in this work. A detailed study of the panchromatic spectrum and habitability potential of Lalande 21185 is in preparation (E. W. Schwieterman et al., 2024, in preparation) and is not included in the sample here. Roughly half of the target stars contained in our study are F- and G-type stars. Table 2 provides a summary of the stellar physical parameters for all stars included in our study, including the effective temperature ($T_{\rm eff}$), spectral type (from R. O. Gray et al. 2006), stellar mass (M), bolometric luminosity ($L_{\rm bol}$), and approximate age (in gigayears). All data were compiled using the NASA Exoplanet Archive.[9] R.A., decl., and distances were taken from Gaia DR3 (Gaia Collaboration et al. 2023). More detailed discussion of each stellar system is provided in Appendix A.

3. X-Ray Data

We retrieved all publicly available imaging observations for our target stars from the XMM-Newton[10] and Chandra[11] archives. Table 3 summarizes the number of observations and the approximate exposure times utilized in this work. Below, we provide a more detail description of how the observations were processed and the methods used to extract light curves and spectra for each facility.

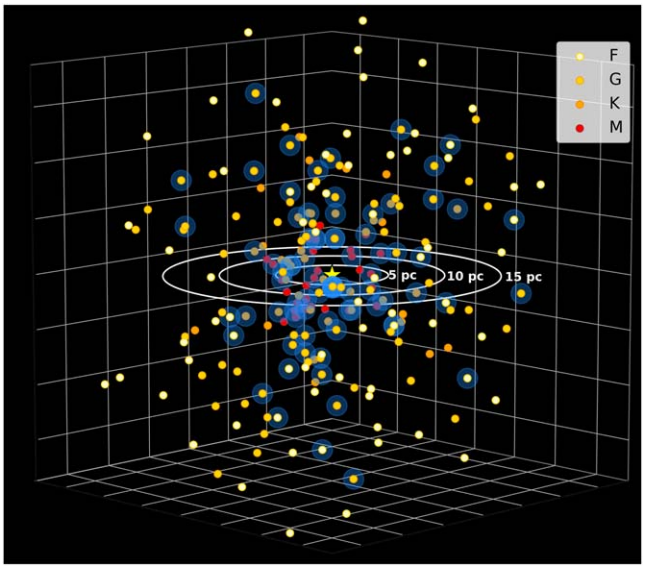

Figure 1. Map of nearby potential direct imaging target stars, color coded by spectral type. Stars with blue halos have available X-ray observations. The yellow star at the center of the diagram represents the Sun, with white concentric rings showing distances of 5 pc, 10 pc, and 15 pc. The animated version of this figure (8 s in duration) shows the 3D distribution through different elevation and azimuthal angles (colors and symbols are the same as the static figure).

(An animation of this figure is available in the online article.)

3.1. XMM-Newton

We retrieved XMM-Newton observations from the XMM-Newton Science Archive and reprocessed the data from the raw `evt1` files using SAS 18.[12] The European Photon Imaging Camera on board XMM-Newton carries a set of three X-ray CCD arrays: one array uses pn-CCDs (referred to as PN) and two utilize metal oxide semiconductor CCDs (referred to as MOS1 and MOS2). The PN data were reprocessed with `epproc`, and the MOS data were reprocessed using `emproc` and filtered on an energy range of 0.2–15 keV. Due to the brightness of many of the stars, pile-up (when two or more photons fall on a pixel in less than the readout time) is a significant concern. The PATTERN parameter records the number and pattern of CCD pixels that are triggered for a given event; we use the recommended PATTERN = 0 to mitigate pile-up effects.[13] Background light curves were extracted using `evselect` and inspected for background flares, and good time intervals (GTIs) were generated to reject observation times exhibiting strong background flaring events.

We inspected the reprocessed, cleaned images for evidence of an X-ray source at the location of the target star. If the target star was detected at $\gtrsim$500 counts in the PN image, we extracted source light curves (binned to 100 s) to search for count-rate variability. We used `evselect` to extract both PN and MOS1/2 spectra for stars with $\gtrsim$2000 net counts, `rmfgen` to generate redistribution matrix files (RMFs), and `arfgen` to generate ancillary response functions (ARFs) for all available

[9] See https://exoplanetarchive.ipac.caltech.edu/.
[10] See https://nxsa.esac.esa.int/nxsa-web/#home.
[11] See https://cda.harvard.edu/chaser/.
[12] https://www.cosmos.esa.int/web/xmm-newton/sas
[13] See the XMM-Newton ABC Guide at https://heasarc.gsfc.nasa.gov/docs/xmm/sl/epic/image/sas_cl.html.

Table 2
Properties of Sample Stars

Star Name	Alternate Name(s)	R.A. (J2000)	Decl. (J2000)	Spectral Type[a]	Distance	Mass	$T_{\rm eff}$	$L_{\rm bol}$	Age*	References
					(pc)	($M_\odot$)	(K)	($L_\odot$)	(Gyr)	
(1)	(2)	(3)	(4)	(5)	(6)	(7)	(8)	(9)	(10)	(11)
η Crv	HIP 61174	12:32:03.75	−16:11:46.55	F2V	17.96 ± 0.17	$1.48^{+0.29}_{-0.19}$	6854^{+124}_{-99}	$4.62^{+0.22}_{-0.25}$	$1.5^{+0.2}_{-0.4}$	(1, 2, 50)
ξ Oph	HIP 84893	17:21:00.68	−21:06:49.81	F2V	17.06 ± 0.10	$1.44^{+0.30}_{-0.20}$	6756^{+110}_{-127}	$4.13^{+0.17}_{-0.18}$	⋯	(1, 2)
υ And A	HD 9826	01:36:47.60	41:24:13.54	F8V	13.41 ± 0.06	1.29 ± 0.04	6157 ± 112	$3.35^{+0.10}_{-0.14}$	3.12	(1, 2, 29)
ι Hor	HR 810, HD 17051	02:42:34.03	−50:47:57.54	F9V	17.32 ± 0.02	$1.17^{+0.17}_{-0.15}$	6146^{+106}_{-184}	$1.74^{+0.04}_{-0.06}$	0.47; 2.72	(1-4, 9)
ν Phe	HIP 5862	01:15:12.13	−45:31:51.14	F9V	15.17 ± 0.04	$1.15^{+0.18}_{-0.14}$	6119^{+130}_{-154}	2.00 ± 0.06	2.88	(1, 2, 3, 9)
γ Pav	HIP 105858	21:26:26.81	−65:21:45.50	F9V	9.27 ± 0.04	$1.15^{+0.18}_{-0.14}$	6109^{+110}_{-176}	1.47 ± 0.05	1, 7.25	(1, 3, 44, 45)
β Vir	HIP 57757	11:50:42.51	01:45:48.67	F9V	$11.12^{+0.07}_{-0.06}$	$1.13^{+0.16}_{-0.14}$	6071^{+120}_{-90}	$3.77^{+0.11}_{-0.14}$	2.96	(1, 2)
GJ 1095	HIP 35136	07:15:50.19	+47:14:20.89	F9V	$16.86^{+0.19}_{-0.20}$	1.12	5866	1.54 ± 0.06	1, 7	(1, 2, 10)
LHS 237	GJ 288, HIP 37853	07:45:34.63	−34:09:53.86	F9V	15.20 ± 0.13	1.11	5744	1.51 ± 0.06	⋯	(1, 2)
ι Per	HIP 14632	03:09:06.10	+49:36:46.35	F9.5V	10.51 ± 0.03	$1.08^{+0.18}_{-0.10}$	5938^{+141}_{-169}	$2.23^{+0.04}_{-0.10}$	4.20 ± 0.48	(1, 2, 9)
β Hyi	HIP 2021	00:25:55.80	−77:15:10.06	G0V	7.47 ± 0.03	$1.14^{+0.01}_{-0.02}$	5839	3.70 ± 0.05	6.32	(1, 2, 9)
β Com	HIP 64394	13:11:51.43	+27:52:55.58	G0V	9.18 ± 0.03	$1.10^{+0.14}_{-0.13}$	5969^{+188}_{-100}	$1.41^{+0.05}_{-0.04}$	<1.12, 1.7	(1, 2, 9)
LHS 208	HD 39091, π Men	05:37:11.89	−80:27:52.05	G0V	18.27 ± 0.02	1.094 ± 0.039	6037 ± 45	1.44 ± 0.02	$2.98^{+1.40}_{-1.30}$	(5)
ρ CrB	GJ 9537, HIP 78459	16:01:02.41	+33:18:00.28	G0V	17.47 ± 0.02	$1.05^{+0.12}_{-0.15}$	5833^{+141}_{-124}	$1.81^{+0.06}_{-0.04}$	11.04	(1, 2, 9)
GL 672	HIP 84862	17:20:39.74	+32:27:47.22	G0V	14.54 ± 0.02	$1.05^{+0.16}_{-0.10}$	5817^{+120}_{-84}	$1.29^{+0.04}_{-0.03}$	12.04	(1, 2, 9)
χ^1 Ori	HIP 27913, GJ 222	05:54:22.76	+20:16:33.07	G0V	8.66 ± 0.08	$1.028^{+0.03}_{-0.028}$	5822	1.17 ± 0.06	0.35; 4.32	(1, 2, 6, 9)
GL 788	HIP 100017	20:17:32.60	+66:51:18.04	G0V	17.57 ± 0.52	1.02 ± 0.03	5886	1.18 ± 0.10	$3.76^{+1.88}_{-1.92}$	(2, 9)
47 UMa	GJ 407, HD 95128	10:59:27.53	+40:25:49.80	G0V	13.80 ± 0.03	1.005 ± 0.047	5829 ± 95	1.58 ± 0.04	$6.48^{+1.44}_{-1.04}$	(9, 29)
GL 620.1A	HD 147513	16:24:01.39	−39:11:34.68	G1V	12.903 ± 0.02	$1.06^{+0.12}_{-0.14}$	5873^{+110}_{-103}	$1.032^{+0.003}_{-0.004}$	2; <1; 0.4	(1–4, 9, 19)
GL 311	π^1 UMa, HD 72905	08:39:11.64	+65:01:16.67	G1.5V	$14.27^{+0.14}_{-0.15}$	1.01	5920	1.03 ± 0.05	0.2	(2, 6, 8)
α Cen A	GJ 559A, LHS 50	14:39:36.49	−60:50:02.37	G2V	1.347 ± 0.003	$1.06^{+0.05}_{-0.04}$	5801	1.61 ± 0.07	$7.84^{+1.08}_{-1.28}$	(2, 9)
44 Boo A	ι Boo, HIP 73695 A	15:03:46.74	+47:39:15.89	G2V	12.8 ± 0.2	1.04 ± 0.1	5877	1.552	1.5	(46, 47, 48)
18 Sco	GJ 616, HIP 79672	16:15:37.52	−08:22:17.91	G2V	14.13 ± 0.02	$1.04^{+0.12}_{-0.14}$	5791^{+117}_{-93}	$1.09^{+0.04}_{-0.02}$	$5.84^{+1.88}_{-1.96}$	(1, 9, 10)
51 Peg	HIP 113357, GJ 882	22:57:28.22	+20:46:08.78	G2V	15.46 ± 0.03	$1.03^{+0.17}_{-0.09}$	5758^{+102}_{-120}	$1.37^{+0.02}_{-0.05}$	6.76	(1, 2)
ζ^1 Ret	LHS 171, HIP 15330	03:17:49.26	−62:34:20.76	G2V	12.12 ± 0.08	$0.96^{+0.03}_{-0.06}$	5699	0.80 ± 0.05	1.56 ± 0.44	(2, 9)
HD 136352	GJ 582, ν^2 Lupi	15:21:45.55	−48:19:07.88	G2V	14.68±0.02	0.87 ± 0.04	5664 ± 61	1.04 ± 0.06	$12.3^{+1.2}_{-2.9}$	(11, 12)
GL 327	HIP 43726	08:54:17.50	−05:26:03.56	G3V	$17.42^{+0.44}_{-0.47}$	1.09 ± 0.04	5790	$1.09^{+0.05}_{-0.04}$	1.32	(2, 9)
μ Ara	HD 160691	17:44:08.68	−51:50:05.65	G3IV/V	15.60 ± 0.03	$1.03^{+0.15}_{-0.11}$	5772^{+119}_{-84}	$1.90^{+0.04}_{-0.06}$	5.7 ± 0.6	(1, 2, 7)
κ^1 Cet	HD 20630	03:19:21.98	+03:22:14.22	G5V	9.14 ± 0.03	$1.02^{+0.16}_{-0.10}$	5712^{+161}_{-124}	$0.86^{+0.02}_{-0.03}$	0.35; 0.7; 2.2	(1, 2, 6, 20, 21)
HD 140901	GL 599	15:47:28.54	−37:55:02.15	G7IV/V	15.25 ± 0.01	1.06 ± 0.05	5587^{+153}_{-125}	1.22 ± 0.03	3.2 ± 2.8	(1, 49)
GJ 777A	LHS 3510, HD 190360	20:03:38.25	+29:53:40.08	G7IV/V	16.01 ± 0.02	0.99 ± 0.08	5552 ± 11	1.20 ± 0.06	13.4	(1, 2, 9)
ξ Boo A	37 Boo, HD 131156	14:51:23.53	+19:06:00.97	G7V	6.71 ± 0.16	0.90 ± 0.04	5551 ± 21	0.55 ± 0.04	<4	(38)
δ Pav	GJ 780	20:08:46.81	−66:11:13.53	G8IV	6.09 ± 0.01	$0.99^{+0.14}_{-0.10}$	5590^{+156}_{-140}	$1.25^{+0.02}_{-0.04}$	6.2	(1, 2
LHS 2156	HIP 47080	09:35:38.55	+35:48:32.33	G8IV/V	11.20 ± 0.02	$0.96^{+0.16}_{-0.09}$	5499^{+156}_{-136}	$0.80^{+0.02}_{-0.04}$	⋯	(1, 2)
82 Eri	GJ 139, HD 20794	03:20:00.08	−43:03:59.59	G8V	6.003 ± 0.009	0.94 ± 0.12	5413^{+91}_{-118}	0.65 ± 0.01	5.76; >12	(1, 2, 9, 13)
τ Ceti	HD 10700, GJ 71	01:44:02.17	−15:56:01.25	G8.5V	3.603 ± 0.007	$0.92^{+0.12}_{-0.10}$	5333^{+124}_{-75}	0.51 ± 0.01	>12	(1, 2, 9)
44 Boo Ba		15:03:46.74	+47:39:15.89	K0V	12.8 ± 0.2	0.98	5300	0.51	⋯	(46, 47, 48)
55 Cnc A	ρ^1 Cnc, HIP 43587	08:52:35.22	+28:19:47.22	K0IV/V	12.59 ± 0.01	$0.90^{+0.14}_{-0.09}$	5252^{+123}_{-172}	0.64 ± 0.02	9.5	(1, 2)
70 Oph A	LHS 458, HIP 88601A	18:05:27.47	+02:29:42.81	K0V	5.15 ± 0.03	0.89 ± 0.02	5300 ± 50	0.65 ± 0.02	6.2 ± 1.0	(1, 22)
40 Eri A	GJ 166A, HD 26965	04:15:13.91	−07:40:05.08	K0.5V	5.04 ± 0.01	$0.85^{+0.11}_{-0.10}$	5092^{+140}_{-149}	0.43 ± 0.01	6.9 ± 4.7	(1, 14, 23)
δ Eri	HIP 17378	03:43:14.80	−09:45:36.30	K1III/IV	9.04 ± 0.07	1.19	5095	$3.37^{+0.07}_{-0.06}$	6.28	(2)
GL 451A	Groombridge 1830	11:53:04.16	+37:41:34.18	K1IV	$9.16^{+0.16}_{-0.17}$	0.66	4950	0.23 ± 0.04	5.0 ± 0.3	(2, 6)

Table 2
(Continued)

Star Name	Alternate Name(s)	R.A. (J2000)	Decl. (J2000)	Spectral Type[a]	Distance	Mass	$T_{\rm eff}$	$L_{\rm bol}$	Age*	References
					(pc)	($M_\odot$)	(K)	($L_\odot$)	(Gyr)	
(1)	(2)	(3)	(4)	(5)	(6)	(7)	(8)	(9)	(10)	(11)
GL 117	HIP 13402, HD 17925	02:52:32.56	−12:46:14.00	K1.5V	10.355 ± 0.005	$0.89^{+0.09}_{-0.13}$	5225^{+91}_{-136}	0.40 ± 0.01	1.5;<1.2;0.1	(1, 2, 6, 9)
α Cen B	GJ 59 B, LHS 51	14:39:35.06	−60:50:15.10	K2IV	1.347 ± 0.03	0.87 ± 0.07	5234 ± 63	0.52 ± 0.05	8, >11	(2, 9, 30)
GL 783 A	HD 191408A, LHS 486	20:11:12.54	−36:06:29.58	K2.5V	6.05 ± 0.03	0.74	4922	0.28 ± 0.10	7.05 ± 0.65	(1, 2, 6, 25)
GL 183	HD 32147, HIP 23311	05:00:49.59	−05:45:30.96	K3V	8.845 ± 0.003	$0.81^{+0.11}_{-0.09}$	4931^{+133}_{-134}	0.29 ± 0.01	2	(1, 3, 6)
GL 892	HD 219134	23:13:21.06	+57:10:10.80	K3V	6.531 ± 0.004	0.79 ± 0.03	4817 ± 62	0.29 ± 0.01	11.0 ± 2.2,12.46	(1, 2, 36)
GJ 667 A	HIP 84709	17:18:56.53	−34:59:25.40	K3V	6.97 ± 0.83	0.59	4810	$0.13^{+0.17}_{-0.09}$	⋯	(2, 3, 31)
LHS 1875	GL 250, HIP 32984	06:52:17.47	−05:10:25.42	K3.5V	8.747 ± 0.004	$0.76^{+0.09}_{-0.10}$	4719^{+157}_{-129}	$0.22^{+0.02}_{-0.01}$	3.1,<0.48	(1, 2, 9)
GL 570 A	HIP 73184	14:57:29.18	−21:25:23.31	K4V	5.881 ± 0.003	$0.75^{+0.08}_{-0.10}$	4681^{+165}_{-126}	$0.22^{+0.01}_{-0.02}$	<0.6;3	(1, 2, 9)
ξ Boo B		14:51:23.19	+19:06:03.97	K4V	6.71 ± 0.16	0.66 ± 0.07	4350 ± 150	0.10 ± 0.02	<4	(38)
44 Boo Bb		15:03:46.74	+47:39:15.89	K4V	12.8 ± 0.2	0.55	5035	0.24	⋯	(46, 47, 48)
GJ 667 B	WDS J17190-3459 B	⋯	⋯	K4V	⋯	⋯	⋯	⋯	⋯	(31)
70 Oph B	LHS 459	18:05:27.82	+02:29:39.12	K5V	5.15 ± 0.03	0.73 ± 0.01	4390 ± 200	0.15 ± 0.02	6.2 ± 1.0	(1, 22)
61 Cygni A	HIP 104214	21:06:59.64	+38:45:49.90	K5V	3.497 ± 0.001	$0.67^{+0.08}_{-0.09}$	4304^{+161}_{-128}	0.15 ± 0.01	6	(1, 2, 26)
61 Cygni B	HIP 104217	21:07:00.88	+38:45:21.86	K7V	3.497 ± 0.001	$0.61^{+0.08}_{-0.09}$	3949^{+156}_{-137}	$0.104^{+0.012}_{-0.009}$	6	(1, 2, 26)
GL 412A	HIP 54211	11:05:22.09	+43:31:51.41	M1V	4.83 ± 0.03	0.38	3688	$0.020^{+0.090}_{-0.014}$	3	(2, 15, 28)
GL 570 B	(HIP 73182)	14:57:27.70	−21:25:07.94	M1.5V	5.86 ± 0.06	0.55 ± 0.05	3345	0.13 ± 0.09	⋯	(1, 2, 37)
GJ 832	LHS 3685, HD 204961	21:33:33.90	−49:00:45.47	M1.5V	4.964 ± 0.001	0.44 ± 0.02	3601	$0.03^{+0.09}_{-0.02}$	9.24	(1, 2, 4)
GJ 667 C		17:19:00.30	−34:59:52.06	M1.5V	7.244 ± 0.005	0.33 ± 0.02	3350 ± 50	0.0137 ± 0.0009	>2	(31)
Kapteyn's Star	GJ 191	05:11:50.38	−45:02:37.73	M2V	3.9331 ± 0.0004	0.28 ± 0.02	3742 ± 157	0.016 ± 0.004	$11.5^{+0.5}_{-1.5}$	(1, 2, 16)
Wolf 1055	HD 180617, GL 752 A	19:16:55.26	+05:10:08.04	M2.5V	5.912 ± 0.02	0.48 ± 0.02	3534 ± 51	0.032 ± 0.001	⋯	(40)
AD Leo	GJ 388	10:19:35.70	19:52:11.30	M3V	4.964 ± 0.001	0.423 ± 0.012	3477 ± 23	0.0236 ± 0.0001	0.4 ± 0.1	(39)
GL 570 C	HIP 73182	14:57:27.70	−21:25:07.94	M3V	5.86 ± 0.06	0.39 ± 0.03	⋯	0.018	⋯	(37)
Wolf 1061	GJ 628, LHS 419	16:30:17.96	−12:40:04.26	M3.5V	4.306 ± 0.001	0.30 ± 0.02	3309 ± 157	$0.011^{+0.003}_{-0.002}$	⋯	(1, 2)
Luyten's Star	GJ 273	07:27:25.11	+05:12:33.78	M3.5V	5.92 ± 0.02	0.29 ± 0.02	3382 ± 49	$0.0087^{+0.0063}_{-0.0065}$	⋯	(1, 2, 43)
55 Cnc B		08:52:40.28	+28:18:54.91	M4.5V	12.48 ± 0.02	0.26 ± 0.02	3187 ± 157	0.008 ± 0.002	⋯	(1, 35)
GL 783B	HD 191408B, LHS 487	20:11:12.80	−36:06:32.17	M4.5V	6.05 ± 0.03	0.24	⋯	0.0009	7.05 ± 0.65	(25)
GJ 777B	LHS 3509	20:03:37.57	+29:53:45.49	M4.5V	15.97 ± 0.01	0.21 ± 0.02	3099 ± 157	0.0047 ± 0.0012	⋯	(1, 34)
40 Eri C	LHS 25	04:15:19.12	−07:40:15.25	M4.5V	5.04 ± 0.01	0.204 ± 0.006	3100	0.008	6.9 ± 4.7	(1, 14, 23, 24)
υ And B		01:36:50.16	41:23:25.98	M4.5V	13.47 ± 0.02	0.19 ± 0.02	3159 ± 157	$0.0044^{+0.0012}_{-0.0011}$	⋯	(29)
Proxima Centauri	GJ 551	14:29:34.16	−62:40:33.87	M5.5V	1.3012 ± 0.0003	0.13 ± 0.02	2900 ± 100	$0.0016^{+0.0004}_{-0.0006}$	4.85	(1, 17, 18)
GL 412B	WX UMa, LHS 39	11:05:24.50	+43:31:33.27	M6.6V	4.83 ± 0.03	0.095	2700	0.00095	3	(27, 28)
VB 10	GL 752 B	19:16:57.61	+05:09:01.59	M8V	5.912 ± 0.02	$0.0881^{+0.0026}_{-0.0024}$	2508^{+63}_{-60}	0.000499±0.000004	1	(41, 42)

References: (1): K. G. Stassun et al. (2019), (2): ExoCat-1 (https://nexsci.caltech.edu/missions/EXEP/EXEPstarlist.html), M. C. Turnbull (2015), (3): R. O. Gray et al. (2006), (4): J. Sanz-Forcada et al. (2010), (5): C. X. Huang et al. (2018), (6): E. E. Mamajek & L. A. Hillenbrand (2008), (7): G. F. Benedict et al. (2022), (8): Gaia Collaboration (2020), (9): G. Takeda et al. (2007), (10): R. O. Gray et al. (2003), (11): L. Delrez et al. (2021), (12): S. Udry et al. (2019), (13): F. Pepe et al. (2011), (14): B. Ma et al. (2018), (15): A. W. Mann et al. (2015), (16): G. Anglada-Escude et al. (2014), (17): J. P. Faria et al. (2022), (18): P. Kervella et al. (2003), (19): L. Ghezzi et al. (2010), (20): J. D. Dorren & E. F. Guinan (1994), (21): M. Güdel et al. (1997), (22): P. Eggenberger et al. (2008), (23): B. D. Mason et al. (2017), (24): H. M. Johnson & C. D. Wright (1983), (25): M. C. Turnbull & J. C. Tarter (2003), (26): P. Kervella et al. (2008), (27): L. Casagrande et al. (2008), (28): A. W. Mann et al. (2015), (29): L. J. Rosenthal et al. (2021), (30): N. C. Santos et al. (2013), (31): G. Anglada-Escudé et al. (2013), (32): W. P. Bidelman (1985), (33): F. Feng et al. (2019), (34): S. L. Hawley et al. (1996), (35): F. J. Alonso-Floriano et al. (2015), (36): M. Gillon et al. (2017), (37): J. M. Mariotti et al. (1990), (38): J. Fernandes et al. (1998), (39): D. Kossakowski et al. (2022), (40): J. Burt et al. (2021), (41): S. H. Pravdo & S. B. Shaklan (2009), (42): J. S. Pineda et al. (2021), (43): N. Astudillo-Defru et al. (2017), (44): J. Holmberg et al. (2009), (45): B. Mosser et al. (2008), (46): H. Zirm (2011), (47): O. Latković et al. (2021), (48): P. Zasche et al. (2009), (49): F. Philipot et al. (2023), (50): B. Nordström et al. (2004).
[a] Significant disagreements in the literature are discussed in Appendix A.

(This table is available in machine-readable form in the online article.)

Table 3
Summary of X-Ray Observations

Star	XMM-Newton		Chandra	
	# Obs.	Exp. Time (ks)	# Obs.	Exp. Time (ks)
η Crv	0	⋯	4	38.5
ξ Oph	0	⋯	1	19.8
υ And	1	5.3	4	58.9
ι Hor	32	211.3	0	⋯
ν Phe	1	16.0	0	⋯
γ Pav	1	15.9	0	⋯
β Vir	1	41.1	0	⋯
GJ 1095	0	⋯	1	96.2
LHS 237	1	15.6	0	⋯
ι Per	0	⋯	1	4.9
Total	151	2235.7	41	815.0

(This table is available in its entirety in machine-readable form in the online article.)

observations. All spectra were binned to contain at least 25 counts per bin.

The majority (∼83%) of the observations analyzed in this work are from the XMM-Newton archive, containing ∼75% of the total exposure time. However, with a spatial resolution of ∼15″, only stellar binaries with angular separations larger than ∼30″ can be resolved with the PN camera. Figure 2 (left panel) shows a 10 ks XMM-Newton/PN image of the binary system GL 412, where the two components (and a third, unidentified X-ray source) are resolved.

3.2. Chandra

We retrieved Chandra ACIS imaging observations from the Chandra archive[14] and reprocessed all `evt1` data using the CIAO v4.15 (A. Fruscione et al. 2006) task `chandra_repro` and standard reduction procedures. We ran the point-source detection algorithm `wavdetect` on each individual exposure to generate a list of X-ray source positions and error ellipses. The major and minor axes of these error ellipses were increased by a factor of 5, and all X-ray sources were masked so that a background light curve could be extracted for each observation. We inspected these background light curves for background flaring events. We created GTIs using `lc_clean` and filtered all event data on these GTIs. Finally, we restricted the energy range of our resulting "clean" `evt2` files to 0.5–7 keV.

We re-ran `wavdetect` on the cleaned image to identify significant X-ray sources and obtain first-pass estimates of their source properties. Due to its exquisite spatial resolution (0.″496 pixel size) and a typical on-axis PSF size $< 1''$ for the ACIS instruments, Chandra is the instrument of choice for resolving crowded fields. For stellar systems with multiple components and angular separations of less than a few arcseconds, Chandra is currently the only telescope that can be used to definitively associate X-ray emission with a given stellar component. Figure 2 (right panel) illustrates the spatial resolving power of Chandra with a 5 ks exposure of the triple star system 40 Eri, where the brightest X-ray source is clearly associated with the position of 40 Eri C, a fainter X-ray source is found at the location of 40 Eri A, and 40 Eri B is undetected.

[14] https://cda.harvard.edu/chaser/

If the target star was detected in the cleaned `evt2` image with $\gtrsim$50 net counts, we extracted source light curves (binned to 100 s) to search for evidence of X-ray variability. For sources with $\gtrsim$500 net counts, the CIAO tool `specextract` was used to extract spectra and generate RMFs and ARFs. All spectra were binned to contain at least 10 counts per bin.

3.3. Swift

The X-Ray Telescope (XRT) on board the Neil Gehrels Swift Observatory additionally observed some nearby stars. Swift is optimized to quickly slew to observe transient events, and typically obtains short "snapshot" X-ray observations (∼2 ks or less) with XRT of relatively bright X-ray sources. These observations are useful for providing flux estimates (or flux upper limits) for stars of interest, but often cannot provide the longer-duration light curves or higher signal-to-noise spectra that can be obtained from XMM-Newton or Chandra. We therefore use the High Energy Astrophysics Science Archive Research Center[15] to determine which stars were observed by Swift but not XMM-Newton or Chandra, and we use the Swift data products generator[16] to create stacked images of these additional stars and measure count rates (or count rate upper limits). The 19 stars that were observed only by Swift/XRT, but not by XMM-Newton or Chandra, are not considered part of our primary stellar sample, but we still provide updated provide X-ray luminosity estimates in Appendix B.

4. Analysis Procedure

We first inspected all X-ray observations for evidence of X-ray emission at the location of the target stars. For stars that were detected, we first extract light curves (binned to 100 s) to search for rapid variability within the observation. For brighter stars (i.e., those with $\gtrsim$2000 net counts with XMM-Newton or $\gtrsim$500 net counts with Chandra), changes in observed count rate are readily apparent by visual inspection; for fainter stars, a more quantitative assessment of variability is needed in addition to visual inspection.

4.1. Assessing Count Rate Variability

We use the Anderson–Darling test, which is a nonparametric statistical test that is more sensitive to short-duration variations than the more commonly used Kolmogorov–Smirnov test (E. D. Feigelson et al. 2022). The Anderson–Darling statistic, A^2, is computed as (M. Rahman & S. Chakrobartty 2004)

$$A^2 = -N - \frac{1}{N}\sum_{i=1}^{N}[(2i-1)\ln(t_i) + (2N+1-2i)\ln(1-t_i)], \quad (1)$$

where N is the number of photons observed, and t_i is the arrival time of the ith bin, scaled to the interval (0, 1). We use `scipy`'s `anderson` routine to compute A^2 and the critical values for the 5% and 1% significance levels when compared to a normal distribution. An A^2 value that is larger than a critical value for a given significance level is evidence of variability; the typical 5% critical value is ∼0.75 and the typical 1% critical value is ∼1.05 for the observations considered here. We

[15] https://heasarc.gsfc.nasa.gov/cgi-bin/W3Browse/swift.pl
[16] https://www.swift.ac.uk/user_objects/index.php

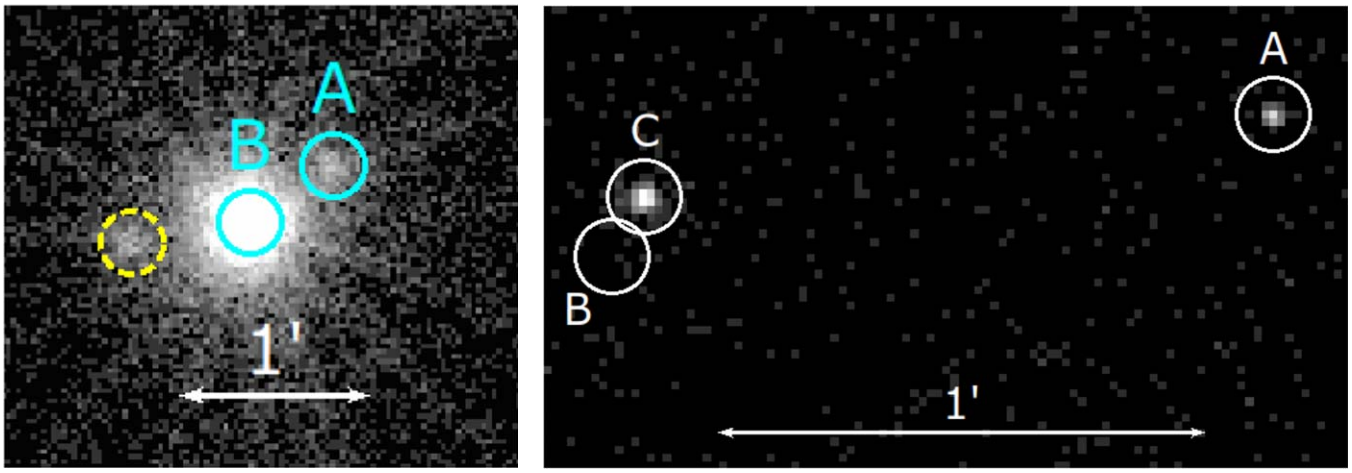

Figure 2. Comparison of the spatial resolution of XMM-Newton (left) and Chandra (right); a 1′ scale bar is shown in both images. Left: the GL 412 binary star system with the locations of GL 412A (M1V) and GL 412B/WX Ma (M6.6V) shown by cyan circles. The circles have radii of 10″ and are separated by ∼30″ . A third, unidentified X-ray source (dashed yellow circle) is located ∼37″ from GL 412B. Right: the 40 Eri triple star system with the locations of 40 Eri A (K0V), 40 Eri B (DA white dwarf), and 40 Eri C (M4.5V) circled in white. The separation between the B and C components is ∼7″. X-ray sources are found coincident with 40 Eri A and C, while 40 Eri B is undetected.

additionally compare the observed light curve to a constant count rate and compute a standard reduced χ^2_r (χ^2 divided by the degrees of freedom) statistic.

Variability in observed count rate is, to first order, driven by a change in X-ray flux incident on the detector. In our case, this change in flux is due to changes in the intrinsic X-ray luminosity of the target star. However, changes in the underlying spectra of the star can additionally impart more subtle changes on the light curve, as the sensitivity of XMM-Newton and Chandra to X-ray photons is energy dependent. We therefore "flag" segments of each light curve according to the type of variability observed, hereafter referred to as the VarFlag, so that the spectral properties can be measured and an accurate count rate-to-luminosity conversion factor can be established as a function of time during the observation. The VarFlags are defined as follows:

1. Q: quiescent periods, when the count rate is low and constant within the uncertainties.
2. F: strong flaring events, where the count rate is above ∼80% of the quiescent maximum count rate.
3. D: decaying periods following flares or descending count rates that follow highly elevated count rates; these periods are roughly defined as immediately following an obvious flare where the count rate is below 80% the maximum flare count rate but still above ∼150% of the quiescent count rate.
4. E: elevated count rate periods, when count rates are approximately 50% higher than the quiescent count rate but not obviously associated with a strong flaring event.
5. R: rising count rate periods that precede a strong flare.

Dividing a single observation into a series of subexposures is a subjective process: we wish to define subexposures that are short enough to capture unique variations seen in the light curve (such as rapid flaring events, some lasting only 200–300 s) but long enough so that a sufficient number of X-ray counts are available for adequate spectral modeling (the ∼2000 and ∼500 count limits for XMM-Newton and Chandra, respectively). Our main goal is to accurately measure the X-ray luminosity of the star as a function of time.

Figure 3 shows an example light curve of Proxima Centauri (XMM-Newton observation number 0801880501) and a cumulative distribution function (CDF) of photon arrival times compared to a constant count rate. The A^2 statistic, critical values, and χ^2_r are shown, and the light curve has been color coded according to the VarFlag assigned to each segment of the light curve. Table 4 summarizes the variability metrics for every X-ray observation of every star available in the archives. While some stars in our sample have been the targets of extensive observing campaigns by XMM-Newton and/or Chandra for many years, observational data is quite sparse for other stars. For stars with many observations, long-term periodic X-ray variability has been detected and is likely the result of coronal activity cycles (e.g., ι Hor, the α Cen system; J. Sanz-Forcada et al. 2019; T. Ayres 2023). Similar long-term X-ray variability cycles may exist for sparsely observed stars in our sample, but will not be detectable in single snapshot observations. Additional observations are required to constrain the long-term coronal activity cycle and/or flaring activity for many stars in the present sample.

4.2. Spectral Modeling

All X-ray spectral modeling was performed with XSPEC v12.11.1 (K. A. Arnaud 1996) using standard χ^2 statistics. Depending on the number of counts and the overall complexity of the spectra, we used one-, two-, or three-temperature APEC models to parameterize the X-ray spectra. Since all of the stars are located very close to the Sun (within ∼20 pc), the intervening hydrogen column density is expected to be low; we adopt a fixed absorbing column $N_{\rm H}$ (using the TBABS model) of 10^{19} cm^{-2} for all stars (a similar assumption was made by A. Brown et al. 2023). We assume abundances from J. Wilms et al. (2000) for both the plasma emission and interstellar absorption models. The plasma temperature and normalizations were left as free parameters during the fit. The normalization of each APEC component is defined as (neglecting cosmological terms)

$$\mathcal{N} = \frac{10^{-14}}{4\pi d^2} \int n_e n_{\rm H} dV, \quad (2)$$

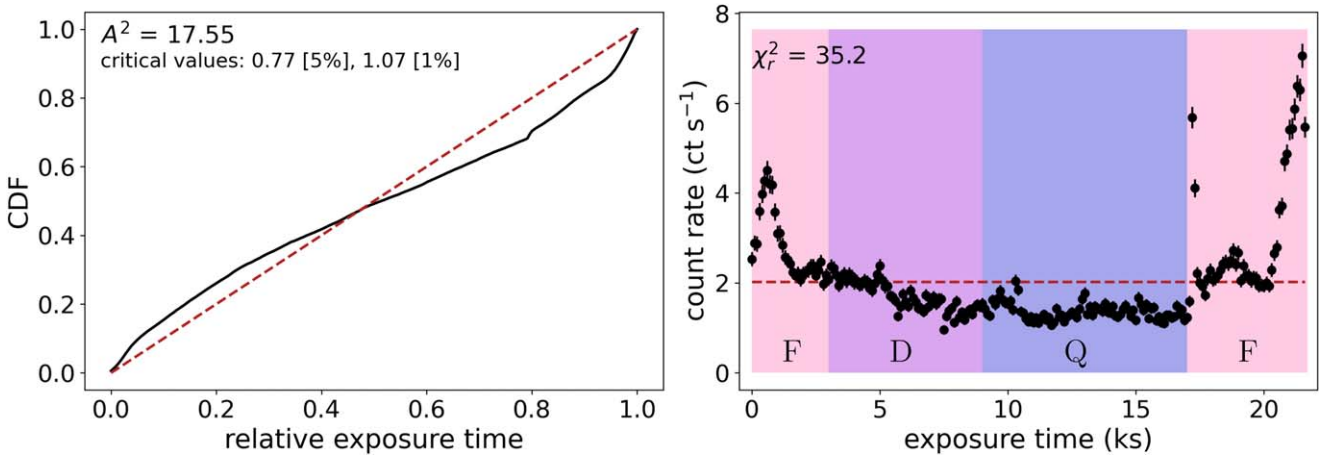

Figure 3. Left: photon arrival time CDF of Proxima Centauri (XMM-Newton observation ID 0801880501, black) compared to a constant count rate (dark red, dashed). The A^2 statistic and critical values are shown in the upper-left corner. Right: the light-curve data (black circles) compared to a constant count rate (dark red, dashed), with sections of the light curve color coded by VarFlag. Quiescent periods are shown in dark blue-violet ("Q"), flaring periods in pink "F"), and descending count rates in purple ("D").

Table 4
X-Ray Variability Metrics

Star	Observation ID	Exp. Time (ks)	Net Counts	χ^2_r	A^2
ι Hor	XMM/0673610201	5.3	4230 ± 70	1.5	0.49
β Vir	XMM/0044740201	41.1	18,450 ± 160	3.1	0.73
υ And A	XMM/0722030101	5.3	940 ± 40	2.1	0.36
44 Boo	XMM/0100650101	18.8	287,110 ± 550	3.1	0.64
GL 620.1A	XMM/0822070201	7.8	12,220 ± 110	1.9	0.41
κ^1 Cet	Chandra/22327	14.0	6600 ± 80	1.7	3.26
Wolf 1061	Chandra/20163	38.3	250 ± 40	0.9	29.78
Prox Cen	XMM/0801880501	20.0	66,790 ± 260	35.2	17.55
GL 412B	XMM/0742230101	10.3	32,030 ± 210	243.1	3.43
VB 10	XMM/0504010101	24.2	660 ± 110	1.1	11.01

Note. Net counts are reported for 0.2–15 keV for XMM-Newton observations and 0.5–7 keV for Chandra observations.

(This table is available in its entirety in machine-readable form in the online article.)

where d is the distance to the source, n_e and $n_{\rm H}$ are the electron and hydrogen column densities (in units of cm^{-3}), respectively, and dV is the volume element (in units of cm^3). The integral $\int n_e n_{\rm H} dV$ is the volume emission measure (VEM). Once the best-fit model is obtained, we use the CFLUX convolution model to measure the flux on each plasma component.

While the spectra of some stars required only one or two APEC components to achieve a statistically acceptable fit, most spectra required a third APEC component. We initialized all spectral models with the default (solar) abundance. For some stars (e.g., ι Hor, κ^1 Cet), the best-fit model was insensitive to the exact choice of abundance; for these stars, the abundance was kept fixed at the solar value. If a statistically acceptable fit was not obtained with solar abundances, we allowed the abundance to be a free parameter of the fit, subject to the constraint that the abundance be the same for all plasma components.

For stars that exhibited count rate variability, spectra were extracted and modeled for each subexposure. Table 5 provides full best-fit parameters for all stars with enough counts to perform spectral modeling for all observations and subexposures. For stars with multiple observations or multiple subexposures with the same VarFlag, we present the average best-fit model for a given VarFlag in Table 6. For uniformity, we refer to the coolest component of a three-component model as "APEC #1," the hottest component as "APEC #3," and the intermediate-temperature component as "APEC #2." The two-temperature thermal plasma models have their individual components matched to the three-temperature component with the most similar temperature. Figure 4 shows an example of the averaged spectrum for ι Hor, which did not exhibit significant count rate variability in any of the publicly available 38 XMM-Newton observations and was therefore assigned a VarFlag of Q (quiescent). The best-fit models for the individual exposures are shown in black, with the average best-fit spectrum superimposed in red.

Figure 5 shows the VEM for each star (calculated from the best-fit normalization, defined in Equation (2) above) as a function of temperature for the coolest APEC component (circles), the intermediate APEC component (squares), and the hottest APEC component (diamonds) using the measurements summarized in Table 6. The points are color coded by stellar spectral type: F and G stars are shown in yellow, K stars in orange, and M stars in red. In general, the temperatures and

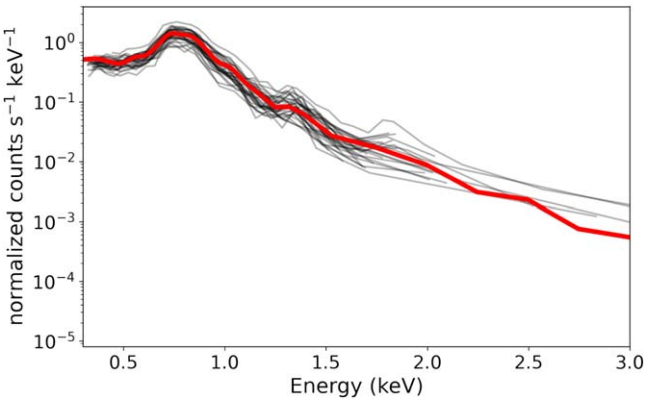

Figure 4. Best-fit spectra for all 38 XMM-Newton observations of ι Hor (black) with the average best-fit spectrum superimposed (red).

VEMs of M stars exhibit the largest spread in coronal temperatures relative to more massive stars. The coronal temperatures of FG and K stars are similar for the coolest and hottest APEC components, although VEMs of FG stars are roughly an order of magnitude higher than those of K stars at similar temperatures. The VEMs do not significantly change within a given spectral type group, but the intermediate-temperature APEC component of FG stars is on average hotter (by ∼2 MK) than the intermediate APEC component of K stars.

The three-component thermal plasma model that generally describes the X-ray emission from F and G stars is described by plasma temperatures of ∼1.3, 5.1, and 9.4 MK, with corresponding (log) VEMs of 55.2, 55.4, and 55.0 cm^3, respectively. For K stars, the temperatures become 1.2, 3.3, and 10 MK, with (log) VEM values of 54.1, 53.9, and 53.6 cm^3, respectively. For these hotter stars, periods of elevated count rates or flaring events differ from the quiescent periods in that VEMs increased, while the plasma temperatures remained mostly constant. This result is in sharp contrast to the model fits for M stars, which showed more significant variations in both temperature and VEM during flaring events.

4.3. X-Ray Luminosity

In addition to insights about the temperatures and VEMs of coronal structures associated with our target stars, the best-fit X-ray spectral models provide us with a count-rate-to-luminosity conversion factor that mitigates against instrumental effects from the extracted light curves and gives us a clearer view of the luminosity evolution of the target star. Furthermore, we can "unfold" our X-ray spectra (i.e., de-convolve the observed spectrum and the energy-dependent detector response function) to assess the intrinsic energy emission from the target star as a function of energy (or wavelength).

Figure 6 shows the continuum luminosity of each star (in units of $L_\odot$) as a function of wavelength during quiescent times. All spectra have been corrected for minor foreground absorption, and we use the XSPEC command `fakeit` to extend our best-fit model to a wavelength range of ∼1–200 Å. For nearly all stars, flaring events are driven by (sometimes dramatic) enhancements in X-ray luminosity at wavelengths $\lesssim$10 Å (energies $\gtrsim$1.2 keV). Figure 7 shows quiescent and flaring spectra for three representative stars (κ^1 Cet, GJ 570A, and Prox Cen) from 1–1000 Å (top panel), as well as the ratio of the flaring and quiescent spectra (bottom panel). For both κ^1 Cet (G5V) and GJ 570A (K4V), the flux at ∼1 Å (∼12 keV) during flaring times is a factor of ∼30 larger than during quiescent times, but the fluxes at longer wavelengths ($\gtrsim$100 Å; energies $\lesssim$0.12 keV) are similar. In the case of Prox Cen (M5.5V), however, the flaring spectrum is brighter than the quiescent spectrum by at least an order of magnitude at all wavelengths, with short-wavelength ($\lesssim$3 Å) emission enhanced by more than a factor of 10^3. This finding is unlikely to be the result of the reduced soft energy responses of Chandra or XMM-Newton, as the loss of effective area due to contamination build-up occurs most significantly at energies below 1 keV (e.g., C. E. Grant et al. 2024). Nevertheless, we use detector response functions specific to the orbital cycle in which the individual observations were obtained to de-convolve the detector response as accurately as possible. Plots of individual stellar X-ray spectra, color coded by VarFlag, are discussed in Appendix A.

A question that our analysis can elucidate is: for what fraction of time is a star observed to be emitting at a given X-ray luminosity? While this is related to the flaring frequency and the typical peak luminosity and duration of flares, our goal in this work is not to directly characterize flaring events or the physical mechanisms that cause them. Rather, we wish to predict the X-ray environments in which HZ planets reside.

To do this, we use our best-fit spectral models to first convert the observed count rates to luminosities. For stars that are too faint to have their spectra directly modeled, we use the spectral model of the star with the closest spectral type and physical parameters to convert the observed count rates into luminosities. For stars that are detected but too faint for reliable light-curve extraction, we simply estimate their time-averaged X-ray luminosity; for undetected stars, we calculate 3σ luminosity upper limits. We then apply Astropy's (Astropy Collaboration et al. 2013, 2018) `bayesian_block` algorithm to the light curves; the "fitness" parameter is used to define the measurement uncertainties. The Bayesian block algorithm (J. D. Scargle 1998; J. D. Scargle et al. 2013) is a segmentation technique, which aims to optimally split (in this case) time series data into "blocks" such that each block is statistically different from its neighboring block. An example Bayesian blocked light curve for κ^1 Cet is shown in Figure 8.

The output of the `bayesian_block` routine is a list of time bins and the luminosity that the star was emitting at during each bin. From these lists, we measure the fraction of the time that each star was observed to be fainter than a given L_X or L_X/L_{bol} value. The results are shown in Figure 9. For comparison, L_X of the modern-day Sun is 6.31×10^{26} erg s^{-1} ($\log L_X/L_{bol} = -6.78$) when quiet and 8.04×10^{27} erg s^{-1} ($\log L_X/L_{bol} = -5.68$) when active (J. L. Linsky et al. 2020), while ∼4 Gyr ago the L_{bol} of the Sun was ∼75% the modern value and its L_X was a factor of ∼2–3 higher (V. N. Obridko et al. 2020). On this plot, a perfectly nonvariable star would be a straight vertical line, while stars that experience significant changes in X-ray luminosity (i.e., Proxima Centauri) will show a pronounced horizontal extent. We measure the luminosities at which the stars spend less than 25%, 50%, 70%, and 90% of the observed time (which we refer to as L_{25}, L_{50}, L_{75}, and L_{90}, respectively). These values are summarized in Table 7; we also include the time-averaged luminosities of faintly detected stars and the 3σ upper limits for nondetected stars in the L_{50} column.

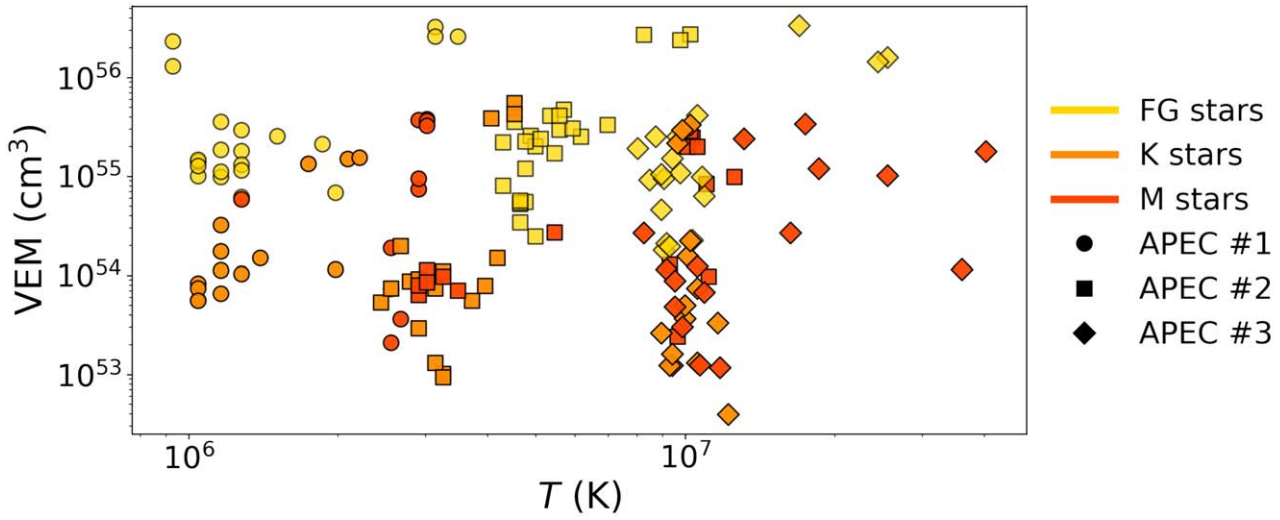

Figure 5. Best-fit VEMs and temperatures for thermal plasma components from XSPEC modeling. VEMs and temperatures from APEC #1 are shown in circles, those from APEC #2 are shown in squares, and those from APEC # are shown in diamonds. Values measured for F and G stars are shown in yellow, K stars in orange, and M stars in red. M stars exhibit the largest variations in both VEM and temperature across all three APEC components.

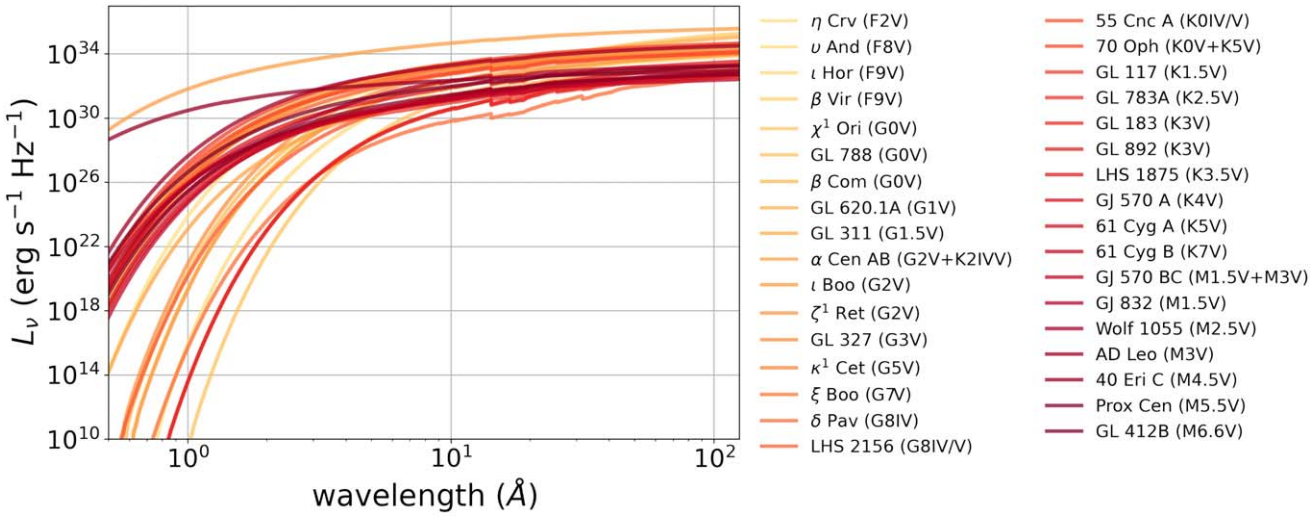

Figure 6. Average continuum quiescent spectra for each target star (0.5–150 Å, corresponding to an energy range of ∼25–0.08 keV). Spectra have been corrected for minor foreground absorption. Stars are color coded by spectral type, with earlier-type stars shown in yellow and later-type stars shown in dark red.

5. Discussion

We compared the 25th and 90th percentile L_X/L_{bol} ratios for stars in our sample to the current minimum and maximum ratios for the Sun (J. L. Linsky et al. 2020), and find that eight stars that were detected in the X-ray observations at high significance exhibit L_X/L_{bol} ratios similar to that of the modern Sun: ξ Oph (F2V), β Vir (F9V), 47 UMa (G0V), β Com (G0V), 55 Cnc A (G8V), GL 892 (K3V), GL 783 (K3V), and GL 183 (K3V). Three of these stars (β Vir, β Com, and GL 183) are younger than the Sun, while four are older (47 UMa, 55 Cnc A, GL 892, and GL 783), and one (ξ Oph) does not have an age estimate available in the literature. Twelve stars have L_X/L_{bol} ratios consistent with those of the early Sun: η Crv (F2V), β Com, GL 311 (G1.5V), ζ^1 Ret (G2V), GL 327 (G3V), HD 140901 (G7IV), the unresolved binary 70 Oph (K0V+K5V), LHS 1875 (K3V), GL 570A (K4V), 61 Cyg A (K5V) and B (K7V), and the unresolved GL 570 BC pair (M1.5V+M3V). We note that one star, β Com, exhibits a range in L_X/L_{bol} that fits within the narrow overlap region between the modern and early Sun ($\log L_X/L_{bol} \approx -6.4$ to -5.7). An additional 11 stars were not detected or only marginally detected and have L_X/L_{bol} upper limits lower than the modern-day minimum solar L_X/L_{bol}: ν Phe, LHS 237, LHS 208, ι Per, ρ CrB, GL 672, 51 Peg, GJ 777A, 82 Eri, GL 451A, and Kapteyn's Star. For roughly a dozen stars in our sample, the observed L_X (or L_X upper limit) translates into X-ray surface fluxes below the $\sim 10^4$ erg s^{-1} cm^{-2} minimum observed in the quiet Sun and other "coronal hole" stars (J. H. M. M. Schmitt 1997). A closer look at these very X-ray faint stars will be the subject of an upcoming study (B. A. Binder et al. 2024, in preparation). In Table 8, we summarize these X-ray-detected solar-like stars (their spectral types and approximate ages are taken from Table 2) and the relevant solar L_X/L_{bol} comparison (modern or early Sun). We additionally provide the "tier" each star was assigned in E. Mamajek & K. Stapelfeldt (2024), indicating the priority that each star should be considered for an HWO direct

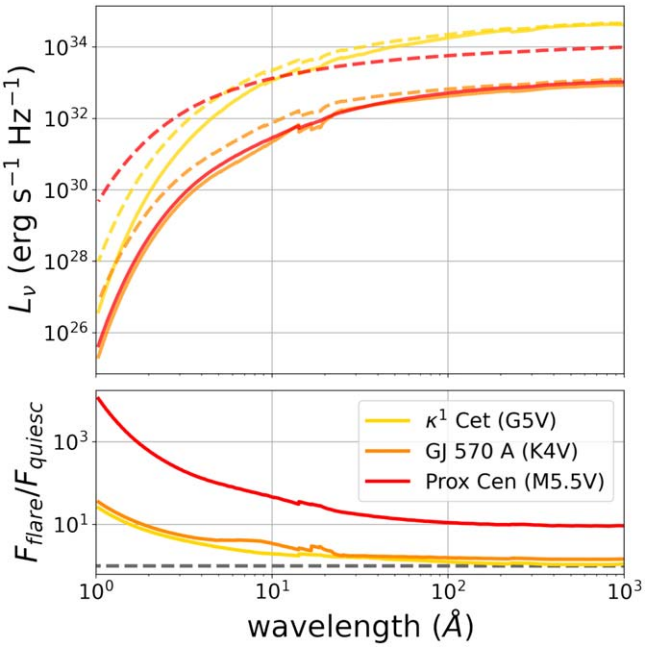

Figure 7. Top: quiescent (solid lines) and flaring (dashed lines) continuum spectra of three representative stars from our sample (κ^1 Cet in yellow, GJ 570 A in orange, and Prox Cen in red). Bottom: the ratio of flaring spectrum to quiescent spectrum, showing a pronounced enhancement in X-ray emission at <10 Å during flaring periods for all three stars. The flaring spectrum of Prox Cen remains an order of magnitude brighter than the quiescent spectrum even at longer wavelengths.

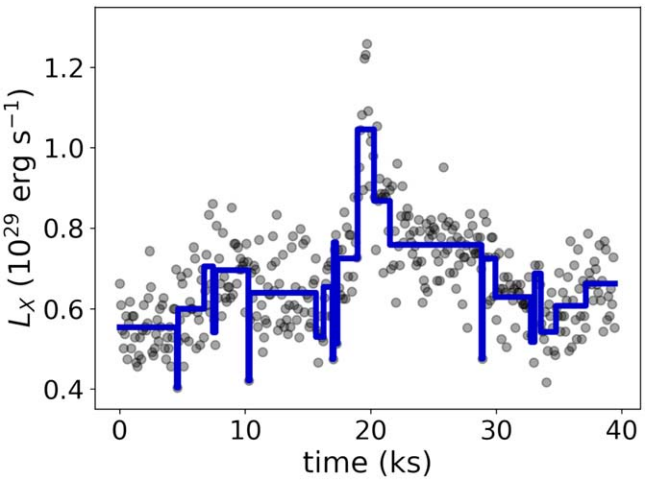

Figure 8. The light curve of κ^1 Cet from XMM-Newton observation 0111410101. The MOS1 count rates were converted to luminosities (gray circles) using the best-fit spectral models from three subexposures (from 0–14 ks, 14–25 ks, and 25–39 ks). The Bayesian blocked light curve is superimposed in blue.

imaging survey (with A indicating the highest priority group, and tiers B and C requiring further study).

Any HZ planets that may exist around the stars listed in Table 8 are currently experiencing high-energy radiation environments that are similar to or less hostile than the modern Earth. Out of the 229 unique stars we identified as potential targets for future direct imaging surveys, only ∼25% had ever been imaged with either XMM-Newton or Chandra (this fraction increases to ∼30% when Swift imaging is included), and out of the 57 stellar systems with high-quality X-ray

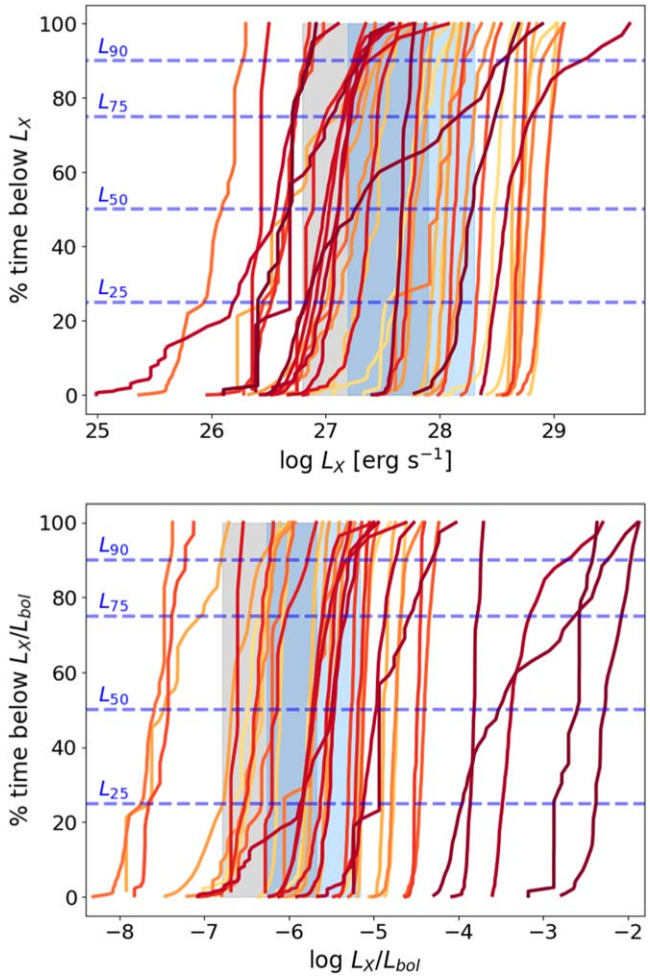

Figure 9. Top: the fraction of time that a star is observed to be fainter than a specific luminosity. Bottom: the fraction of time that a star is observed to be below an L_X/L_{bol} value. Stars are color coded by spectral type, with earlier-type stars shown in yellow and later-type stars shown in dark red. The 25th, 50th, 75th, and 90th percentile luminosities and L_X/L_{bol} ratios are indicated by blue dashed lines (values for each star summarized in Table 7). The shaded gray region indicates typical ranges for the current Sun, and the blue shaded regions indicate approximate ranges for the early Sun (∼4 Gyr ago; see the text).

observation, we find that 28 systems (∼50%) have L_X/L_{bol} ratios similar to or less than that of either the modern or early Sun. These stars span the full range of spectral types and ages considered here, and represent all three tiers of the E. Mamajek & K. Stapelfeldt (2024) ranking system. It is therefore likely that there are an additional ∼100 potential direct imaging target stars with HZs with current X-ray radiation environments similar to or even less hostile than that of the Sun. We note that threshold L_X/L_{bol} ratios below that of the modern or early Sun could be a conservative condition for finding habitable planets. However, the past evolution of the star would also have to be taken into account. Detailed coupled geological and atmospheric evolution analyses would be most informative for predicting the targets with the best chances of maintaining potentially habitable conditions (e.g., J. Krissansen-Totton & J. J. Fortney 2022). A systematic X-ray survey of these as-of-yet unobserved nearby stars is needed to inform the selection of the best targets for direct imaging surveys.

In general, M stars exhibit significantly more X-ray variability than earlier-type stars and spend a significant

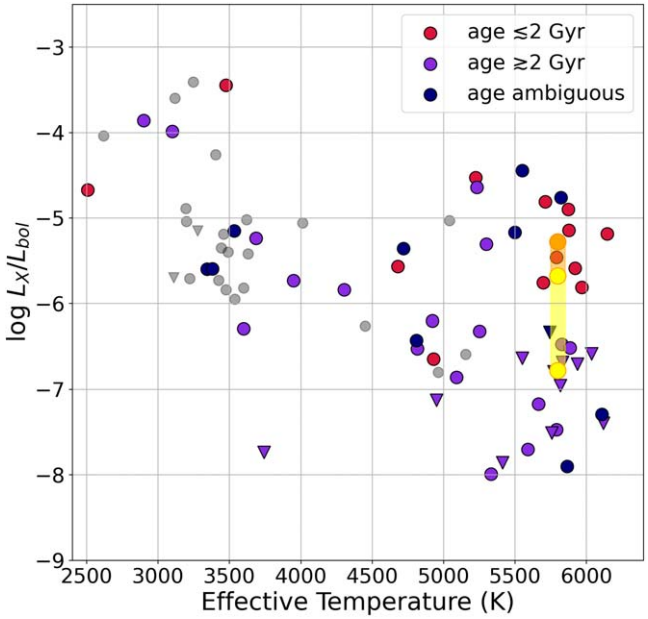

Figure 10. The L_X/L_{bol} ratio as a function of T_{eff}. Stars in our sample with firm X-ray detections are shown in circles, while upper limits are shown for stars that were not X-ray detected (downward pointing triangles). Stars that are believed to be young ($\lesssim$2 Gyr) are shown in red, older stars ($\gtrsim$2 Gyr) are shown in purple, and stars without age estimates or with ambiguous/discrepant age estimates are shown in dark blue. The MUSCLES/Mega-MUSCLES sample (A. Brown et al. 2023) is shown in gray. The yellow circles and shaded area indicate the quiescent and flaring L_X/L_{bol} ratios for the Sun (J. L. Linsky et al. 2020).

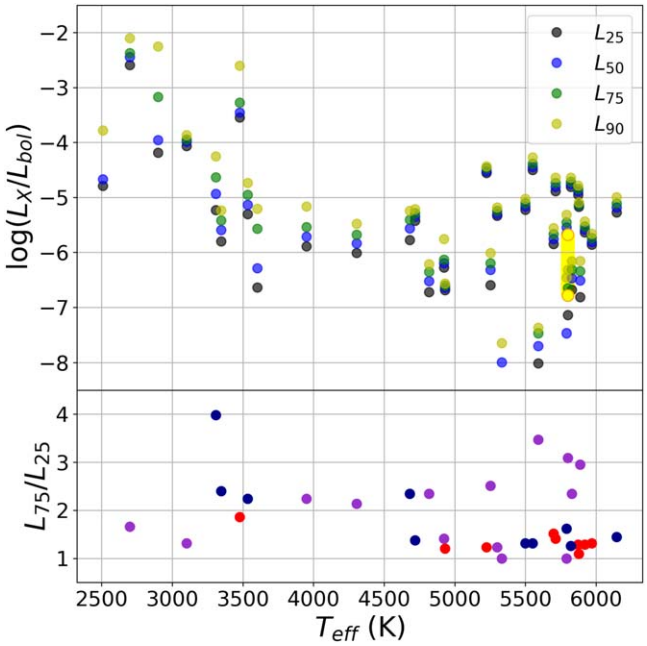

Figure 11. Top: the L_X/L_{bol} ratio as a function of T_{eff} assuming L_{25} (black), L_{50} (blue), L_{75} (green), and L_{90} (dark yellow). The yellow circles and shaded area indicate the quiescent and flaring L_X/L_{bol} ratios for the Sun (J. L. Linsky et al. 2020). Bottom: the ratio of L_{75}/L_{25} as a function of T_{eff}, color coded by age (as in Figure 10: young stars are shown in red, old stars are shown in purple, and stars with ambiguous ages are shown in dark blue).

amount of time at L_X/L_{bol} ratios dramatically larger than that of the Sun. We can supplement our sample of Sunlike and low-mass stars with X-ray observations of an 23 additional M- and K-type stars from the MUSCLES/Mega-MUSCLES survey (A. Brown et al. 2023). A. Brown et al. (2023) found a major decrease in the X-ray-to-bolometric luminosity ratio (L_X/L_{bol}) with increasing effective temperature. We compute L_X/L_{bol} (or upper limits, in the case of X-ray nondetections) for all stars in our sample using L_{50} from Table 7 and L_{bol} from Table 2. In Figure 10, we plot the (logarithmic) L_X/L_{bol} ratio as a function of T_{eff} (also from Table 2) for our full sample (colored points), with the MUSCLES/Mega-MUSCLES sample shown in gray. Our sample extends this inverse relationship between L_X/L_{bol} and T_{eff} by ~1000 K in T_{eff}, with L_X/L_{bol} ratios that are about an order of magnitude lower than observed for K and M stars.

There is a small clustering of stars with $T_{eff} \sim 5200$–6200 K with significantly higher L_X/L_{bol} ratios than the majority of comparable stars, likely due to young stellar ages. Chromospheric activity in solar-type stars is observed to decrease rapidly after ~2–3 Gyr (G. Pace & L. Pasquini 2004; J. Zhang et al. 2019), after which activity levels remain mostly constant. We indicate the approximate age of each star in Figure 10: young stars ($\lesssim$2 Gyr) are shown in red, older stars ($\gtrsim$2 Gyr) are shown in purple, and stars without age estimates or ambiguous ages are shown in dark blue. Most of these high-L_X/L_{bol}, high-T_{eff} stars are indeed believed to be consistent with the younger ages where each spectral type emits elevated high-energy emission (T. Richey-Yowell et al. 2023). There are three stars with ambiguous ages that lie within this region of the diagram (χ^1 Ori, 55 Cnc A, and GL 451A); the observed X-ray emission of these stars suggests that younger age estimates may be preferred for these stars.

In Figure 11 we again show the L_X/L_{bol} ratio as a function of T_{eff} for stars in our sample, but we use L_{25}, L_{50}, L_{75}, and L_{90} to compute the L_X/L_{bol} ratio. This allows us to assess the degree to which intrinsic X-ray variability contributes to the scatter in L_X/L_{bol} observed in Figure 10. The ratio of L_{75}/L_{25} provides an estimate of how much a star varies "normal" about the median L_X. We find that the variability of the youngest stars in our sample exhibit the smallest dynamic range, with $L_{75}/L_{25} \sim 1.3$ for stars with $T_{eff} \gtrsim 5000$ K (for the coolest young star in the plot, AD Leo, $L_{75}/L_{25} \sim 1.8$). The L_{75}/L_{25} ratio for older stars shows more dispersion, varying by up to a factor of ~3.5.

6. Conclusions

We have analyzed ~3 Ms of high-quality XMM-Newton and Chandra observations of 57 nearby stellar systems, as well as snapshot Swift images of an additional 19 stellar systems, to provide a uniform catalog of the X-ray properties of potential target stars for future direct imaging surveys. All X-ray light curves and spectroscopic data are publicly available on Zenodo at doi:10.5281/zenodo.11490574. The X-ray environments in the HZs around F, G, and early-K stars are more likely to be similar to those that the Earth has evolved in, and we identify 29 stars with current L_X/L_{bol} ratios similar to or less than that of the Sun. Our results are consistent with T. Richey-Yowell et al. (2023), who found that the X-ray fluxes of late-M stars can be a factor of ~3–15 times larger than for K stars. In addition to high average L_X/L_{bol} ratios, M stars exhibit more frequent and dramatic flares than earlier-type stars. We note that, of the 229 candidate target stars for direct imaging, only ~30% have been observed by XMM-Newton, Chandra, or Swift.

Table 5
All Best-Fit Parameters from X-Ray Spectral Modeling

Star	ObsID	VarFlag	APEC #1		APEC #2		APEC #3		$\log L_X$ [erg s^{-1}]	Abund	$\langle\chi^2/\mathrm{dof}\rangle$
			kT_1 (keV)	$\mathcal{N}_1$ (10^{-4})	kT_2 (keV)	$\mathcal{N}_2$ (10^{-4})	kT_3 (keV)	$\mathcal{N}_3$ (10^{-4})			
η Crv	14474	Q	$0.16^{+0.07}_{-0.14}$	$3.3^{+10.0}_{-1.6}$	0.50 ± 0.08	$4.6^{+5.0}_{-2.9}$	⋯	⋯	28.43 ± 0.06	$0.32^{+0.56}_{-0.16}$	1.14
β Vir	0044740201	Q	0.09 ± 0.01	$4.7^{+1.2}_{-0.9}$	0.37 ± 0.01	2.4 ± 0.1	⋯	⋯	28.08 ± 0.02	1 (fixed)	2.48
χ^1 Ori	0111500101/0-10ks	E	0.10 ± 0.02	$39.7^{+55.7}_{-19.9}$	0.49 ± 0.03	$52.9^{+10.5}_{-9.4}$	$0.84^{+0.10}_{-0.09}$	$12.1^{+7.8}_{-4.8}$	$28.88^{+0.03}_{-0.04}$	$0.31^{+0.07}_{-0.05}$	1.31
β Com	0148680101/0-5ks	Q	0.07 ± 0.02	$23.5^{+114.8}_{-15.1}$	0.39 ± 0.02	3.4 ± 0.3	⋯	⋯	28.11 ± 0.02	1 (fixed)	1.55
44 Boo	0100650101/0-6ks	D	0.25 ± 0.02	$23.8^{+4.4}_{-6.6}$	$0.50^{+0.13}_{-0.12}$	$9.8^{+5.4}_{-3.6}$	$0.91^{+0.03}_{-0.02}$	$275.3^{+13.8}_{-15.7}$	28.67 ± 0.01	0.09 ± 0.01	1.45
GL 620.1A	0822070301	Q	$0.11^{+0.02}_{-0.01}$	$9.5^{+5.3}_{-3.6}$	0.46 ± 0.03	$1.4^{+2.5}_{-2.3}$	$0.77^{+0.05}_{-0.04}$	$6.3^{+1.9}_{-1.7}$	28.82 ± 0.03	$0.43^{+0.09}_{-0.06}$	1.60

(This table is available in its entirety in machine-readable form in the online article.)

Table 6
Average Best-Fit Parameters from X-Ray Spectral Modeling

Star	VarFlag	APEC #1		APEC #2		APEC #3		$\log L_X$ [erg s^{-1}]	Abund	$\langle\chi^2/\mathrm{dof}\rangle$
		kT_1 (keV)	$\mathcal{N}_1$ (10^{-4})	kT_2 (keV)	$\mathcal{N}_2$ (10^{-4})	kT_3 (keV)	$\mathcal{N}_3$ (10^{-4})			
η Crv	Q	$0.20^{+0.12}_{-0.09}$	$2.3^{+4.3}_{-1.1}$	$0.55^{+0.09}_{-0.07}$	$3.1^{+2.2}_{-1.7}$	⋯	⋯	$28.41^{+0.05}_{-0.10}$	$0.27^{+0.61}_{-0.18}$	1.31
υ And A	Q	0.29 ± 0.03	0.8 ± 0.1	⋯	⋯	⋯	⋯	27.57 ± 0.03	1 (fixed)	0.91
ι Hor	Q	0.09 ± 0.03	7.7 ± 1.1	0.42 ± 0.08	2.9 ± 0.2	0.71 ± 0.14	1.6 ± 0.2	$28.75^{+0.10}_{-0.14}$	1 (fixed)	1.27
β Vir	Q	0.09 ± 0.01	$4.7^{+1.2}_{-0.9}$	0.37 ± 0.01	2.4 ± 0.1	⋯	⋯	28.08 ± 0.02	1 (fixed)	2.48
χ^1 Ori	Q	0.08 ± 0.03	258 ± 228	0.42 ± 0.07	28.6 ± 9.2	0.69 ± 0.06	21.3 ± 8.2	$28.94^{+0.07}_{-0.10}$	0.20 ± 0.12	1.55

(This table is available in its entirety in machine-readable form in the online article.)

Table 7
X-Ray Luminosities and L_X/L_{bol} Ratios (or 3σ Upper Limits) for All Sample Stars

Star	$\log L_{25}$ (erg s^{-1})	$\log L_{50}$ (erg s^{-1})	$\log L_{75}$ (erg s^{-1})	$\log L_{90}$ (erg s^{-1})	$\log(L_{25}/L_{bol})$	$\log(L_{50}/L_{bol})$	$\log(L_{75}/L_{bol})$	$\log(L_{90}/L_{bol})$
η Crv	28.19	28.39	28.47	28.59	−6.06	−5.86	−5.78	−5.66
ξ Oph	27.47	27.64	27.77	28.03	−6.73	−6.56	−6.43	−6.17
υ And A	27.27	27.55	27.72	27.87	−6.84	−6.56	−6.39	−6.24
β Vir	27.90	27.99	28.05	28.15	−6.26	−6.17	−6.11	−6.01
β Hyi	26.23	26.53	26.94	27.37	−7.92	−7.62	−7.21	−6.78
κ^1 Cet	28.63	28.71	28.78	28.88	−4.89	−4.81	−4.74	−4.67
HD 140901	27.62	27.92	28.05	28.23	−6.05	−5.75	−5.62	−5.44
δ Eri	26.39	26.53	26.69	26.89	−7.72	−7.58	−7.42	−7.22
GL 570 A	27.15	27.36	27.52	27.68	−5.78	−5.57	−5.41	−5.25
61 Cyg A	26.75	26.92	27.08	27.28	−6.00	−5.84	−5.68	−5.56
61 Cyg B	26.69	26.87	27.04	27.42	−5.89	−5.71	−5.54	−5.35
AD Leo	28.42	28.51	28.69	29.36	−3.54	−3.45	−3.27	−2.98
Proxima Centauri	26.70	26.93	27.71	28.63	−4.09	−3.86	−3.08	−2.33

(This table is available in its entirety in machine-readable form in the online article.)

Table 8
Potential HWO Target Stars with Solar-like L_X/L_{bol} Ratios

Star Name	Spectral Type	Age (Gyr)	Sun Comparison	HWO Tier
η Crv	F2V	<2	early	C
ξ Oph	F2V	unknown	modern	C
ν Phe	F9V	∼3	<modern min	B
β Vir	F9V	∼3	modern	C
LHS 237	F9V	unknown	<modern min	none
ι Per	F9.5V	∼4	<modern min	A
LHS 208	G0V	∼3	<modern min	B
ρ CrB	G0V	∼11	<modern min	B
GL 672	G0V	∼12	<modern min	C
47 UMa	G0V	∼6.5	modern	A
β Com	G0V	<2	modern,early	A
GL 311	G1.5V	<2	early	B
ζ^1 Ret	G2V	<2	early	A
51 Peg	G2V	∼7	<modern min	none
GL 327	G3V	<2	early	C
GJ 777A	G7IV/V	∼13	<modern min	B
HD 140901	G7IV/V	∼3	early	C
82 Eri	G8V	∼6	<modern min	B
70 Oph AB	K0V+K5V	∼6	early	B
55 Cnc A	K0IV/V	∼9.5	modern	C
GL 451A	K1IV	∼5	<modern min	C
GL 783	K2.5V	∼7	modern	B
GL 892	K3V	∼11	modern	A
GL 183	K3V	∼2	modern	B
LHS 1875	K3.5V	<3	early	C
GL 570A	K4V	<3	early	A
61 Cyg AB	K5V+K7V	∼6	early	A
GL 570 BC	M1.5V +M3V	<3	early	none
Kapteyn's Star	M2V	∼11	<modern min	none

(This table is available in machine-readable form in the online article.)

Acknowledgments

This work is supported by NASA Exoplanets Research Program (XRP) award No. 80NSSC23K0039 (PI Turnbull). This research has made use of the NASA Exoplanet Archive, which is operated by the California Institute of Technology, under contract with the National Aeronautics and Space Administration under the Exoplanet Exploration Program. B. B. is grateful for the warm hospitality of the University of California, Santa Barbara Kavli Institute for Theoretical Physics, where the majority of this manuscript was written; this research was supported in part by grant No. NSF PHY-2309135 to the Kavli Institute for Theoretical Physics. S.P. acknowledges support from NASA under award No. 80GSFC21M0002. E.S. and S.P. acknowledge support from the CHAMPs (Consortium on Habitability and Atmospheres of M-dwarf Planets) team, supported by the National Aeronautics and Space Administration (NASA) under grant Nos. 80NSSC21K0905 and 80NSSC23K1399 issued through the Interdisciplinary Consortia for Astrobiology Research (ICAR) program. This work has made use of data from the European Space Agency (ESA) mission Gaia (https://www.cosmos.esa.int/gaia), processed by the Gaia Data Processing and Analysis Consortium (DPAC, https://www.cosmos.esa.int/web/gaia/dpac/consortium). Funding for the DPAC has been provided by national institutions, in particular the institutions participating in the Gaia Multilateral Agreement. This work made use of data supplied by the UK Swift Science Data Centre at the University of Leicester. We would like to thank Eric Mamajek for useful discussions related to this work, and the anonymous reviewer for providing helpful comments that improved our paper.

Facilities: CXO, XMM, Swift (XRT), Exoplanet Archive

Software: astropy (Astropy Collaboration et al. 2013, 2018, 2022).

Appendix A
Discussion of Individual Stars

In this Appendix, we provide additional context for each stellar system (e.g., when there is a notable discrepancy in the published literature with regards to a given physical parameter) and summarize the known or candidate exoplanets associated with each star. We then present the results of our X-ray analysis for each stellar system. Table 9 summarizes the observations of faint/nondetected stars, including if the star was detected in a given observation or not, the count rate (or upper limit on the count rate) and detection significance, and the "match star" that was used to convert count rates to luminosities.

Table 9
Summary of Faint Star Observations

Star	Observation ID	Detected?	Count Rate (counts s^{-1})	Significance (σ)	Match Star
ξ Oph	Chandra/27852	Yes	$(8.1 \pm 1.0) \times 10^{-3}$	8.0	η Crv
ν Phe	XMM/0206540101	No	$<4.3 \times 10^{-3}$	⋯	ι Hor
γ Pav	XMM/0670380101	Yes	$(1.1 \pm 0.4) \times 10^{-2}$	2.8	ι Hor
GJ 1095	Chandra/4199	Yes	$(2.1 \pm 0.7) \times 10^{-4}$	2.9	ι Hor
LHS 237	XMM/0840210501	No	$<3.7 \times 10^{-2}$	⋯	ι Hor
LHS 208	XMM/0865400201	No	$<1.4 \times 10^{-2}$	⋯	GL 620.1A
LHS 208	Chandra/22293	No	$<5.7 \times 10^{-4}$	⋯	GL 620.1A
ι Per	Chandra/12338	No	$<1.2 \times 10^{-2}$	⋯	ι Hor
ρ CrB	Chandra/12396	No	$<3.8 \times 10^{-3}$	⋯	ι Hor
GL 672	Chandra/12397	No	$<2.1 \times 10^{-3}$	⋯	GL 620.1A
47 UMa	XMM/0304203401	Yes	$(3.9 \pm 0.3) \times 10^{-2}$	12.1	GL 620.1A
β Hyi	Chandra/12337	Yes	$(5.1 \pm 0.6) \times 10^{-2}$	12.5	GL 620.1A
β Hyi	XMM/0006010401	Yes	$(5.6 \pm 0.4) \times 10^{-2}$	14.0	GL 620.1A
18 Sco	XMM/0303660101	Yes	$(2.2 \pm 0.3) \times 10^{-2}$	7.3	GL 311
18 Sco	Chandra/12393	Yes	$(5.5 \pm 1.1) \times 10^{-4}$	5.0	GL 311
μ Ara	XMM/0551021001	No	$<1.6 \times 10^{-2}$	⋯	GL 327
μ Ara	XMM/0551023101	No	$<2.2 \times 10^{-2}$	⋯	GL 327
HD 136352	XMM/0884680201	Yes	$(4.1 \pm 1.5) \times 10^{-3}$	2.7	κ^1 Cet
51 Peg	XMM/0551020901	No	$<2.3 \times 10^{-3}$	⋯	κ^1 Cet
51 Peg	Chandra/10825	No	$<3.1 \times 10^{-3}$	⋯	κ^1 Cet
GJ 777A	XMM/0304201101	No	$<1.2 \times 10^{-2}$	⋯	δ Pav
GJ 777A	XMM/0304202601	No	$<7.8 \times 10^{-3}$	⋯	δ Pav
HD 140901	Chandra/13769	Yes	$(8.9 \pm 0.9) \times 10^{-3}$	11.0	δ Pav
82 Eri	XMM/0670380601	No	$<1.2 \times 10^{-2}$	⋯	55 Cnc A
82 Eri	Chandra/22292	No	$<8.1 \times 10^{-4}$	⋯	55 Cnc A
GL 451A	Chandra/9931	No	$<4.9 \times 10^{-4}$	⋯	GL 183
τ Cet	XMM/0670380501	Yes	$(1.2 \pm 0.2) \times 10^{-2}$	7.0	55 Cnc A
τ Cet	Chandra/1886	Yes	$(2.4 \pm 0.3) \times 10^{-3}$	8.0	55 Cnc A
δ Eri	XMM/0205720101	Yes	$(7.8 \pm 1.1) \times 10^{-3}$	7.3	55 Cnc A
40 Eri A	Chandra/13644	Yes	$(1.4 \pm 0.2) \times 10^{-2}$	7.7	GL 117
GL 412 A	XMM/0742230101	Yes	$(5.7 \pm 0.2) \times 10^{-2}$	28.5	GJ 832
GJ 667 C	Chandra/17317	Yes	$(5.7 \pm 0.9) \times 10^{-3}$	6.3	GJ 832
GJ 667 C	Chandra/17318	Yes	$(3.1 \pm 0.5) \times 10^{-4}$	6.2	GJ 832
Kapteyn	Chandra/merged	No	$<1.2 \times 10^{-4}$	⋯	Wolf 1055
Luyten	Chandra/20164	Yes	$(3.5 \pm 0.7) \times 10^{-3}$	5.0	AD Leo
υ And B	XMM/0722030101	No	$<3.2 \times 10^{-2}$	⋯	40 Eri C
VB 10	XMM/0504010101	Yes	$(2.7 \pm 0.5) \times 10^{-2}$	5.4	GL 412B
VB 10	Chandra/616	Yes	$(1.2 \pm 0.8) \times 10^{-3}$	1.5	GL 412B
VB 10	Chandra/7428	Yes	$(1.6 \pm 0.4) \times 10^{-3}$	4.0	GL 412B

(This table is available in machine-readable form in the online article.)

Figure 12 shows X-ray images of resolved and unresolved binary star systems included in our study. Individual images are discussed further for each star below. Figure 13 shows the light curves extracted for all stars from all observations in which they were detected, with subexposures colored by VarFlag. Figure 14 shows the average best-fit spectra for all sufficiently bright stars. For stars that exhibit flaring events, we also show the ratio of the flaring-to-quiescent spectra as a function of wavelength.

A.1. η Crv

There are no significant discrepancies in the stellar physical parameters of η Crv. Although there are no known or candidate exoplanets, the system is known to host two debris disks: one at a distance of ∼160–180 au, and a hotter disk at ∼3–7 au (M. C. Wyatt et al. 2005, 2007; R. Smith et al. 2008).

η Crv was observed four times with Chandra. All observations were taken with ACIS-S in 1/4 subarray mode for ∼10 ks. In all observations, η Crv was detected with ∼1000 net counts (0.5–7 keV), but no significant variability was observed in the X-ray light curves (see Figure 13). The spectrum of η Crv is well described by a two-component thermal plasma model, with no significant changes in the temperatures or normalizations across the different observations.

A.2. ξ Oph

There are no significant discrepancies in the stellar physical parameters of ξ Oph, and the star does not host any no known or candidate exoplanets. ξ Oph was observed once with Chandra/ACIS-S for 19.8 ks and robustly detected with ∼160 counts (8σ significance). There are hints of low-level variability

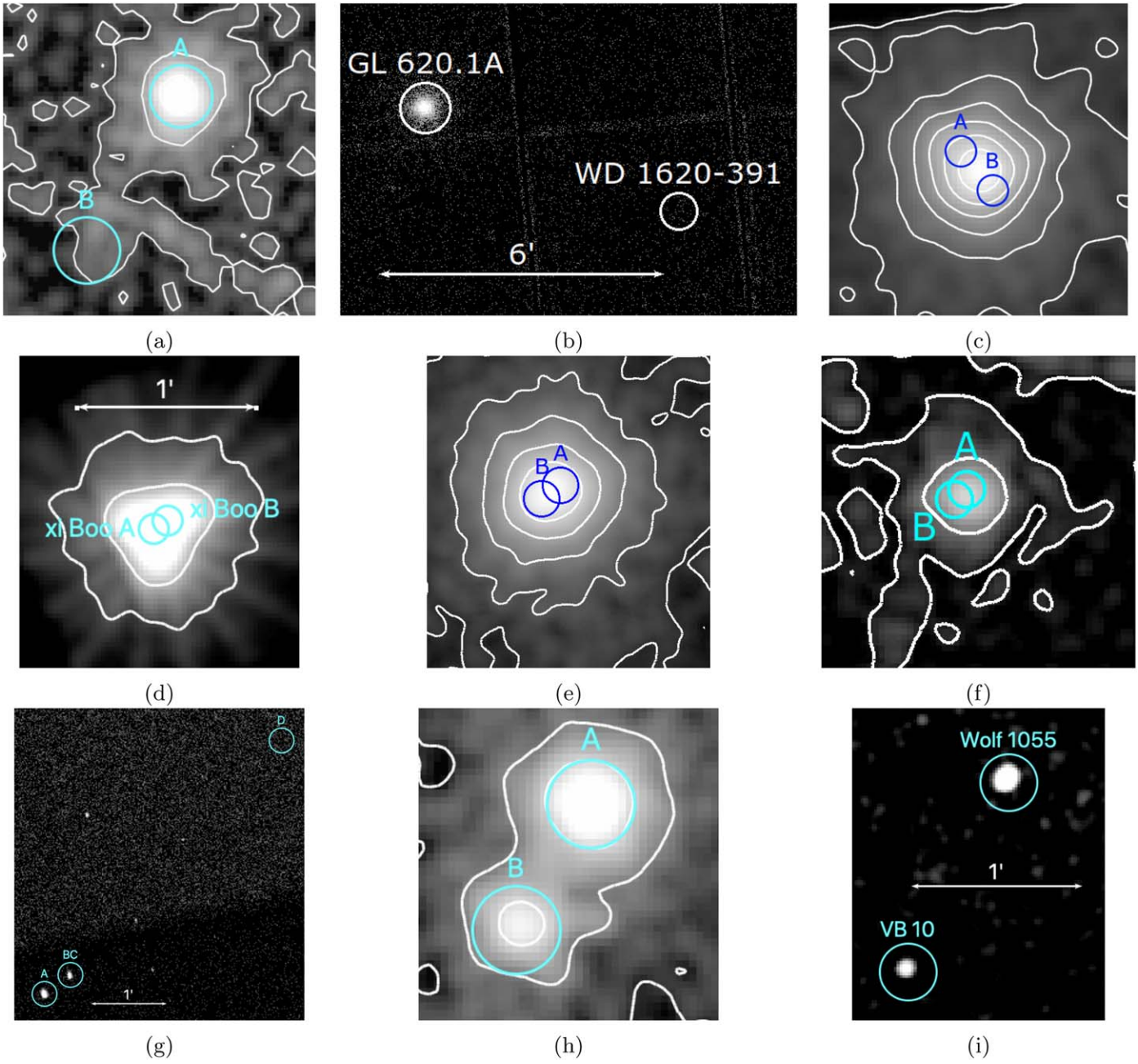

Figure 12. Images of resolved and unresolved binary systems with XMM-Newton and Chandra. (a) XMM-Newton/PN image of υ And. The locations of the F8V star (A) and the M4.5V star (B) are shown by cyan circles (both with radii 10″). The stars are separated by ∼0.′9. (b) XMM-Newton image of GL 620.1A and the white dwarf WD 1620-391. No X-rays are detected at the location of WD 1620-391 in either observation. (c) The α Cen binary system as seen by the PN camera on XMM-Newton. The positions of the G2V star (A) and K1V star (B) are shown in blue circles (both with radii of 5″ and separated by ∼18″). (d) The ξ Boo binary system as seen by the MOS2 camera on XMM-Newton. The locations of the G8V star (A) and K4V star (B) are shown in cyan circles (both with radii of 5″). (e) The 70 Oph binary star system as seen by the PN camera on XMM-Newton. The positions of the K0V star (A) and the K5V star (B) are shown in blue circles (both with radii of 5″ and separated by ∼3.″7). (f) The GL 783 binary star system as seen by the PN camera on XMM-Newton. The positions of the K3V star (A) and the M4.5V star (B) are shown in cyan circles (both with radii of 5″ and separated by ∼2.″6 . (g) Chandra image of the GL 570 system. The primary GL 570A (K4V) is easily resolved from the binary red dwarf pair GL 570BC (M1.5V and M3V, respectively). Cyan circles have a radius of 10″. The brown dwarf GL 570D is not detected in X-rays. (h) The 61 Cyg binary system as seen by the PN camera on XMM-Newton. The positions of the K5V star (A) and K7V star (B) are shown in cyan circles (both with a radius of 10″ and separated by ∼12″). (i) Chandra image of Wolf 1055 and VB 10 (both circles have radii of 10″ and are separated by ∼1.′2). Some images have been smoothed for display purposes only; white contours indicate the intensity distribution of X-ray counts on the detector.

in the X-ray emission of ξ Oph, but the relatively low number of net counts prohibits spectral modeling.

A.3. υ And

υ And A is an F8V dwarf in a presumed binary system with a proper-motion companion υ And B, an M4.5V dwarf (also referred to as υ And D). The two stars have an angular separation of ∼0.′9 (corresponding to ∼750 au). There are no significant discrepancies in the physical parameters of either star. υ And A hosts three confirmed exoplanets (υ And b, c, and d), which were discovered via RV measurements. The masses of υ And b, c, and d are $M_{\rm p} \sin i$ ∼0.67 $M_{\rm Jup}$, ∼0.67 $M_{\rm Jup}$, ∼2 $M_{\rm Jup}$, and ∼4 $M_{\rm Jup}$, respectively, with orbital periods (orbital

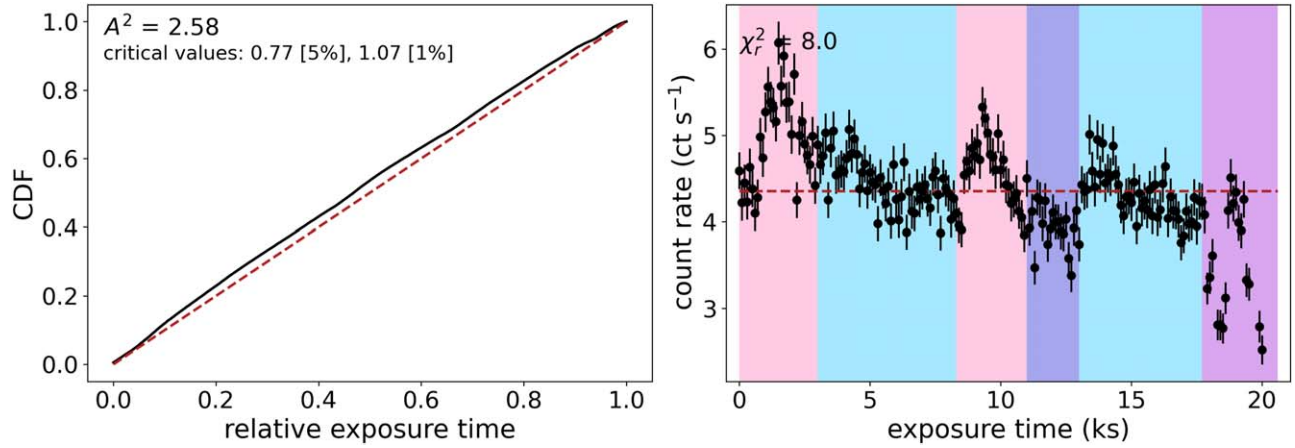

Figure 13. Left: photon arrival time CDF for α Cen (black) compared to a constant count rate (dark red, dashed). The A^2 statistic and critical values are shown in the upper-left corner. Right: the light-curve data (black circles) compared to a constant count rate (dark red, dashed). Quiescent periods are shown in blue-violet, flaring periods in pink, elevated count rate periods in blue, and descending periods in purple. The figure set includes all of the observations in Table 4 with the same ordering. (The complete figure set (201 images) is available in the online article.)

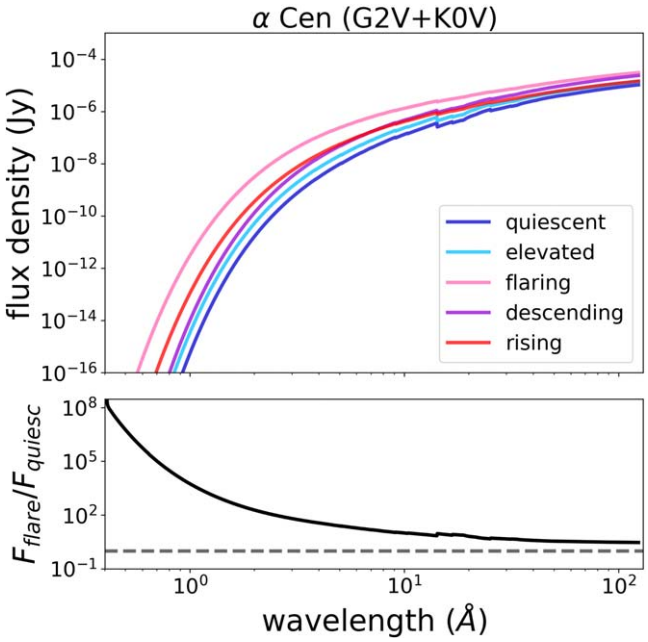

Figure 14. Top: the best-fit continuum spectra for α Cen color coded by VarFlag. Quiescent periods are shown in dark blue, elevated count rate periods in light blue, flaring periods in pink, periods of descending count rates in purple, and periods of rising count rates in red. Bottom: the ratio of the flaring-to-quiescent spectrum as a function of wavelength.
(The complete figure set (18 images) is available in the online article.)

distances) of ∼4.6 days (0.06 au), ∼241 days (0.82 au), and ∼1282 days (2.5 au), respectively (all planetary data taken from L. J. Rosenthal et al. 2021).

The υ And system was observed four times with Chandra/ACIS-S in 1/8-subarray mode (for ∼15 ks per observation) and once with XMM-Newton for 5.3 ks. υ And A was detected in all five observations with sufficient counts to extract light curves (see Figure 13) and with enough counts in Chandra observations 10976 and 10977 to enable spectral modeling. There is no evidence for strong X-ray variability in any observation, and both Chandra spectra were consistent with a single-temperature thermal plasma model with a temperature of ∼0.3 keV (∼3.4 MK; see Table 6). υ And B was out of the field of view of the Chandra observations. However, the star was within the field of view of the XMM-Newton PN detector but fell just on the gap between two CCDs and was not detected (see Figure 12).

A.4. ι Hor

ι Hor is characterized either as a late-F type (F9V; R. O. Gray et al. 2006) or early-G type (G0V; M. C. Turnbull 2015) star. There is additional disagreement on the age of the system: M. C. Turnbull (2015) quoted an age of 2.72 Gyr, while J. Sanz-Forcada et al. (2010) suggested a much younger age of ∼0.47 Gyr (see also the detailed analysis of J. Sanz-Forcada et al. 2019, where an age of 600 Myr was adopted). We adopt a spectral type of F9V and an age of 0.47 Gyr in this work. ι Hor hosts one confirmed exoplanet that was first detected via radial velocity (RV) measurements by M. Kürster et al. (2000). It is a giant planet with $M_p \sin i \sim 2.3\ M_{Jup}$ and an orbital period of ∼300 days (corresponding to an orbital distance of ∼0.9 au; K. G. Stassun et al. 2017).

ι Hor is one of the most thoroughly observed stars in our sample, with 32 publicly available XMM-Newton observations taken between 2011 and 2018. A detailed study of the coronal activity and structure of the star is presented in J. Sanz-Forcada et al. (2019), who combined the XMM-Newton monitoring with observations from TESS and the STIS instrument on the Hubble Space Telescope. They corroborate a 1.6 yr X-ray activity cycle for the star, although ι Hor does not exhibit the same type of dramatic changes in luminosity as seen in other stars in our sample (see Figure 9). Our X-ray analysis of ι Hor is consistent with J. Sanz-Forcada et al. (2019), although we do not undertake a more extensive study of the abundances of the star. Light curves of ι Hor are shown in Figure 13, and the best-fit spectrum is described in Table 6.

A.5. ν Phe

ν Phe is characterized either as a late-F type (F9V; R. O. Gray et al. 2006) or early-G type (G0V; M. C. Turnbull 2015) star. There are no confirmed or candidate exoplanets in the system, and the star was undetected in a 16 ks XMM-Newton observation.

A.6. γ Pav

γ Pav is a known F-type star, with the specific spectral type ranging from F9V (R. O. Gray et al. 2006) to F7V (M. C. Turnbull 2015). There are significant discrepancies in the estimated age of γ Pav: J. Holmberg et al. (2009) quoted an age of ∼1 Gyr based on photometric observations and comparison to stellar evolution models, while an asteroseismic analysis by B. Mosser et al. (2008) yielded an age of 7.25 Gyr. There are no known or candidate exoplanets orbiting γ Pav. The star was only marginally detected (2.8σ) in a 25.9 ks XMM-Newton observation. The low X-ray luminosity of γ Pav is consistent with the older age estimate of B. Mosser et al. (2008).

A.7. β Vir

There are no significant discrepancies in the stellar physical parameters for β Vir, and the star does not host any currently known or candidate exoplanets. β Vir was observed once with XMM-Newton (observation ID 0044740201) and was detected with ∼18,450 net counts on the PN camera (thick filter). The X-ray light curve does not show evidence of significant variability (see Figure 13). The spectrum is well described by a two-temperature thermal plasma model (see Table 6).

A.8. GJ 1095

The spectral type of GJ 1095 is given as F9V by R. O. Gray et al. (2003) or G0V by M. C. Turnbull (2015). There are no known or candidate exoplanets orbiting GJ 1095. The star was only marginally detected (2.9σ) in a 96.2 ks Chandra observation.

A.9. LHS 237

There are no significant discrepancies in the stellar physical parameters of LHS 237, and no age estimate is currently available in the literature. LHS 237 is a triple-star system: the inner spectroscopic binary has an orbital period of ∼10 yr (the angular separation of ∼0.″3 is unresolvable by XMM-Newton; A. Tokovinin 2012), and the third component is one of the coolest known white dwarfs (NLTT 18141 = GJ 288B) located ∼14.′5 from the central binary (J. B. Holberg et al. 2013). There are no known or candidate exoplanets in the system.

LHS 237 was serendipitously imaged by XMM-Newton for 15.6 ks in observation 0840210501 (the intended target for the observation was a Wolf–Rayet star). The inner spectroscopic binary is not detected, and the white dwarf is outside the XMM-Newton field of view.

A.10. ι Per

There are no significant discrepancies in the stellar physical parameters for ι Per. The spectral type is either F9.5V (R. O. Gray et al. 2003) or G0V (M. C. Turnbull 2015). There are no known or candidate exoplanets in the system. ι Per was observed for 4.9 ks with Chandra in ACIS-S 1/4 subarray mode, but the star was not detected.

A.11. β Hyi

There are no significant disagreements in the stellar physical parameters of β Hyi, and the star does not host any currently known or candidate exoplanets. β Hyi was observed once with Chandra/ACIS-S in 1/4 subarray mode and once with XMM-Newton. The star was detected in both observations with sufficient counts to extract light curves, but the star is too faint for accurate spectral modeling to be performed. There is no strong evidence for X-ray variability in either the Chandra or XMM-Newton light curves of β Hyi (see Figure 13).

A.12. β Com

There are only minor differences in the reported age of β Com: G. Takeda et al. (2007) reported an age <1.12 Gyr, while M. C. Turnbull (2015) reported an age of 1.7 Gyr. All other spectral parameters are taken from K. G. Stassun et al. (2017). There are currently no known or candidate exoplanets orbiting β Com.

β Com was robustly detected (with ∼38,000 net counts) in a 57.2 ks observation by XMM-Newton. We extracted a light curve from this observation and found marginal evidence for count rate variability (see Figure 13). Given the large number of counts available, we split the observation into 5 ks-long subexposures and extracted spectra from each subexposure to search for evidence of underlying spectroscopic variability. Throughout the observation, a two-temperature thermal plasma model was sufficient to describe the X-ray spectrum of β Com, with the best-fit temperatures and normalizations remaining constant within the uncertainties. All best-fit subexposure spectral parameters for β Com are provided in Table 5, and the average best-fit spectral parameters are listed in Table 6. The best-fit spectral models are shown in Figure 14.

A.13. LHS 208 (π Men)

All spectral parameters for LHS 208 are taken from C. X. Huang et al. (2018). LHS 208 hosts three confirmed exoplanets. HD 390931 b is a giant planet that was detected via RV measurements (H. R. A. Jones et al. 2002); it has $M_p \sin i \sim 12\ M_{Jup}$ and an orbital period of ∼2090 days (corresponding to an orbital distance of ∼3.3 au; F. Feng et al. 2022). π Men c is a super-Earth that was discovered via transits (D. Gandolfi et al. 2018); it has an $M_p \sin i \sim 3.5\ M_\oplus$ with an orbital period of ∼6 days (∼0.07 au orbital distance; F. Feng et al. 2022). π Men d was detected via RV measurements with $M_p \sin i \sim 13\ M_\oplus$ and an orbital period of ∼125 days (A. P. Hatzes et al. 2022). LHS 208 not detected in a 36.9 ks observation with XMM-Newton or a 19.6 ks observation with Chandra.

A.14. ρ CrB

Some minor discrepancies, mass ranges from 0.95 (J. M. Brewer et al. 2023) to 1.05 $M_\odot$ (K. G. Stassun et al. 2017) and spectral type from G0V (R. O. Gray et al. 2006) to G2V (M. C. Turnbull 2015). ρ CrB hosts three confirmed exoplanets (ρ CrB c, d, and e), with the existence of a fourth exoplanet controversial (ρ CrB b; J. M. Brewer et al. 2023; this may simply be the result of correlated stellar activity in the RV measurements;). The masses of ρ CrB c, d, and e are $M_p \sin i$ ∼28 $M_\oplus$, ∼22 $M_\oplus$, and 3.8 $M_\oplus$, respectively, with orbital periods of ∼102 days (∼0.4 au), ∼282 days (∼0.8 au), and ∼13 days (∼0.11 au), respectively. ρ CrB is also approaching the end of its main-sequence lifetime, with a prognosis of planetary engulfment for most of the known planets in the system (S. R. Kane 2023). ρ CrB was observed once with Chandra/ACIS-S for 9.8 ks, but was not detected.

A.15. GL 672

There are no significant discrepancies in the stellar physical parameters for GL 672, and there are no known or candidate exoplanets in the system. GL 672 was observed for 9.9 ks by Chandra/ACIS-S but was not detected.

A.16. χ^1 Ori

χ^1 Ori is a G0V-type star in a ∼14 yr elliptical ($e \sim 0.45$) orbit with a low-mass companion. RV measurements compiled by I. Han & G. Gatewood (2002) were used to infer a secondary mass of ∼0.15 $M_\odot$ with a likely spectral type of M4V or M5V. The estimated angular semimajor axis of the orbit is ∼0.″668, unresolvable by XMM-Newton but potentially spatially resolvable by Chandra (see Section 3). The inferred spectral parameters may be biased due to the presence of this low-mass companion. There is significant disagreement in the literature about the age of the system. M. C. Turnbull (2015) and G. Takeda et al. (2007) estimated an age of 4.32 Gyr, while E. E. Mamajek & L. A. Hillenbrand (2008) used activity-rotation diagnostics to estimate an age of 300–400 Myr. There are no confirmed or candidate exoplanets in the system.

Since only one XMM-Newton observation is available for χ^1 Ori, we are unable to identify the source of the X-ray emission—whether it be from the G0V star, the low-mass companion, or both. There is one potential, minor flaring event during the observation, starting ∼21 ks after the beginning of the observation and lasting for ∼4 ks, where the peak count rate exceeds the median count rate by ∼40% (see Figure 13). While this may not be a bona fide flare event, we classify this period as flaring so that its spectrum can be compared to the remainder of the observation. The light curve otherwise shows a count rate that is either constant within the uncertainties (which we classify as quiescent) or somewhat elevated above the median count rate level by ∼20% (which we classify as elevated).

Figure 14 shows the quiescent, elevated, and potential flare spectra for the χ^1 Ori system. The elevated and flare spectra are nearly indistinguishable, and both show excess emission over the quiescent spectrum at wavelengths $\lesssim$10 Å. This difference in short-wavelength emission is driven primarily by the hottest thermal plasma component in our model, which has a temperature of ∼0.8 keV for the elevated and flaring spectra but ∼0.7 keV in the quiescent spectrum (see also Table 6). The integrated X-ray luminosity of χ^1 Ori is constant within the uncertainties across the three spectra.

A.17. GL 788

There are no significant discrepancies in reported stellar parameters of GL 788. The system does not host any known or candidate exoplanets. GL 788 was detected in a 9.6 ks XMM-Newton observation with ∼4470 net counts. There was no evidence of count rate variability apparent in the X-ray light curve (see Figure 13). The spectrum was well described with a single, cool thermal plasma ($kT \sim 0.2$ keV).

A.18. 47 UMa

There are no significant discrepancies in the stellar physical parameters reported in the literature for 47 UMa. The star hosts three confirmed giant exoplanets that were detected via radial velocity measurements. 47 UMa b, c, and d have masses of $M_p \sin i \sim 2.4$, ∼0.5, and 1.5∼2.4 M_{Jup}, respectively, and have orbital periods (distances) of ∼1077 days (∼2 au), ∼2287 days (∼7.8 au), and ∼19,000 days (∼12.4 au), respectively. All planetary parameters were taken from L. J. Rosenthal et al. (2021).

47 UMa was detected at ∼12σ significance in a 6.2 ks XMM-Newton observation. We extracted a light curve from the observation but found no evidence of variability (see Figure 13), and the star was too faint to enable spectroscopic modeling.

A.19. GL 620.1A

GL 620.1A is either comoving with (M. Mugrauer 2019) or in a wide binary with (J. B. Holberg et al. 2002) the DA-type white dwarf WD 1620-391. The angular distance between the two components is ∼5.′8, which would correspond to a physical separation of ∼4500 au at the distance of GL 620.1A. GL 620.1A is classified as a barium star, and its overabundance in *s*-process elements has been attributed to pollution due mass transfer during the white dwarf progenitor's AGB phase (G. F. Porto de Mello & L. da Silva 1997). There is some disagreement in the literature over the spectral type and age of GL 620.1A. Spectral types range from G1V (R. O. Gray et al. 2006) to a later G3/5V (M. C. Turnbull 2015); we adopt a spectral type G1V. While M. C. Turnbull (2015) quoted an age of 2 Gyr, other estimates of the age of GL 620.1A are lower: L. Ghezzi et al. (2010) and G. Takeda et al. (2007) derived upper limits of <1 and <0.68 Gyr, respectively, while J. Sanz-Forcada et al. (2010) adopted an age of 0.4 Gyr. One giant exoplanet is confirmed via RV measurements of GL 620.1A (M. Mayor et al. 2004); the planet has $M_p \sin i \sim 1.2\ M_{Jup}$ and an orbital period of ∼528 days (orbital distance of ∼1.3 au).

GL 620.1A is detected in both publicly available XMM-Newton observations (Figure 12) with sufficient counts to enable spectral modeling (see Figure 14 and Table 6). There is no significant variability present in the count-rate light curves of GL 620.1A (Table 4; see Figure 13), so we do not attempt to divide the observations into subexposures.

A.19.1. The White Dwarf WD 1620-391

While GL 620.1A is robustly detected in both publicly available XMM-Newton observations, WD 1620-391 is not (see Figure 12(a)). The 3σ upper limits on the count rates of 0.014 counts s^{-1} (observation ID 0822070201) and 0.0236 counts s^{-1} (observation ID 0822070301). We use WebPIMMs[17] to convert the observed XMM-Newton/PN count rates (both observations were taken with the thick filter) to a flux assuming an APEC thermal plasma model with $kT \approx 0.5$ keV (the approximate best-fit model for the accreting white dwarf G 29-38, which is detected in X-rays by both XMM-Newton and Chandra; T. Cunningham et al. 2022; S. Estrada-Dorado et al. 2023). We find flux (luminosity) upper limits of 2.0×10^{-14} erg s^{-1} cm^{-2} (4×10^{26} erg s^{-1}) and 3.4×10^{-14} erg s^{-1} cm^{-2} (6.8×10^{26} erg s^{-1}) for observations 0822070201 and 0822070301, respectively. These luminosity limits are a factor of ∼5–7 higher than the observed luminosity of G 29-38; targeted observations with a more sensitive X-ray instrument are needed to determine if WD 1620-391 is emitting

[17] See https://heasarc.gsfc.nasa.gov/cgi-bin/Tools/w3pimms/w3pimms.pl.

X-rays at a level comparable to other X-ray-detected white dwarfs.

A.20. GL 311 (π^1 UMa)

There are no significant discrepancies in the stellar physical parameters reported in the literature for GL 311. The system does not host any currently known or candidate exoplanets.

The variability metrics for GL 311 (see Table 4) suggest that count rate variability is observed in the available XMM-Newton observation (observation No. 0111400101; see Figure 13). There are two minor flare-like events in the light curve. The first begins at ∼21 ks after the beginning of the observation, and reaches a peak count rate that is a factor of ∼2 higher than the median count rate. This event lasts for approximately 8 ks, and it is immediately followed by a second count rate increase, which exceeds the median count rate by a factor of ∼1.6 and lasts for approximately 5 ks. The post-flare count rate is elevated by ∼15% relative to the pre-flare count rate. Spectroscopic modeling before, during, and after the flaring event shows that the temperatures of all three thermal components increased in temperature during the flaring event, although a modest decrease in the normalization (related to the VEM) during the flare led to a constant (within the uncertainties) luminosity (Figure 14; see also Table 6).

Thus, although GL 311 clearly exhibits a degree of rapid X-ray variability (on a timescale of a few hours), this activity does not have a significant affect on the overall X-ray luminosity output of the star. The relative stability of the star's X-ray luminosity is also apparent in Figure 9, where the luminosity curve for GL 311 is near vertical.

A.21. α Cen

α Centauri A (G2V) and B (K1V) are members of the extensively studied triple system that also includes Proxima Centauri (M5.5V; see Section A.56). α Cen A and B are in a ∼80 yr elliptical orbit (e∼0.5; R. Akeson et al. 2021). One candidate exoplanet, α Cen B b, was reported (X. Dumusque et al. 2012) but was later found to be a false-positive signal (V. Rajpaul et al. 2016). There are currently no other known or candidate exoplanets in the α Cen AB system.

The semimajor axis of the α Cen system is ∼18″, but due to the brightness of the stars, there is considerable blending in the XMM-Newton images (see Figure 12). We therefore do not attempt to extract X-ray products (light curves, spectra) for each star individually. The α Cen system exhibits significant X-ray variability (see Figure 13). The system is well described by a three-component thermal plasma model, and increases in the observed count rates are driven largely by increases in the hottest plasma temperature (from ∼0.6 keV during quiescent periods to ∼0.8–0.9 keV during times associated with flaring events) and normalization (which increases by a factor of ∼12). The spectra of α Cen are shown in Figure 14 (see also Table 6). Due to the significant blending of the two components, we do not use the quiescent α Cen spectrum as a baseline for inferring other stellar luminosities.

A.22. 44 Boo

44 Boo (also called ι Boo) is a triple star system with a G0V primary (44 Boo A) in ∼210 yr orbit with a spectroscopic binary composed of a K0V (44 Boo Ba) dwarf and a K4V (44 Boo Bb) dwarf (P. Zasche et al. 2009; H. Zirm 2011). 44 Boo A is separated from the spectroscopic binary by ∼0.″2. The 44 Boo B binary has an orbital period of only ∼6.4 hr and is a possible contact binary (W. Lu et al. 2001). There are no known or candidate exoplanets in the 44 Boo system.

44 Boo is robustly detected with XMM-Newton in an 18.8 ks observation, with count-rate variations clearly seen in the light curve (see Figure 13). We do not include the final ∼5 ks in our spectral analysis due to a significant background flaring event during the observation. Our spectral modeling revealed no significant differences between the minor flaring event from ∼6–10 ks, and the relatively constant count rate period from 15–20 ks. The spectrum of 44 Boo did change during periods of declining count rate (the first 6 ks and from 10–15 ks) as the result changes in the hottest thermal plasma component: kT_3 decreased from ∼2.1–2.2 keV during quiescent/flaring times to ∼1.5 keV during periods of secular decline, while the normalization of this component (related to the VEM) more than doubled. These changes to APEC #3 result in a decrease in X-ray flux at the shortest wavelengths ($\lesssim$10 Å); see Table 6 and Figure 14.

A.23. 18 Sco

There are minor differences in the reported spectral type of 18 Sco: M. C. Turnbull (2015) quoted a spectral type of G5V, but R. O. Gray et al. (2006) classified the star as a G2V. We adopt a spectral type of G2V. 18 Sco hosts one candidate super-Earth with $M_p \sin i \sim 6.8\ M_\oplus$ and an orbital period of ∼20 days (K. Laliotis et al. 2023). The star is detected in both a 20.1 ks XMM-Newton observation and a 62.2 ks observation with Chandra/ACIS-S. However, the 18 Sco is not bright enough in either observation for timing or spectroscopic analysis to be performed.

A.24. 51 Peg

There are no significant discrepancies reported for the stellar parameters of 51 Peg. The star is famous for hosting the first discovered exoplanet (M. Mayor & D. Queloz 1995), the hot Jupiter 51 Peg b with $M_p \sin i \sim 0.46\ M_{Jup}$ and an orbital period of ∼4.2 days (∼0.05 au L. J. Rosenthal et al. 2021). 51 Peg was observed with both Chandra and XMM-Newton, but was not detected in either observation.

A.25. ζ Ret

The wide binary ζ Ret contains ζ^1 Ret, which is listed as a G3V/G5V by M. C. Turnbull (2015) but G2V as R. O. Gray et al. (2006), and ζ^2 Ret, a G2V star (E. F. del Peloso et al. 2000). The two stars are separated by ∼5.′2 . The system does not hot any known or candidate exoplanets.

Although this separation would be easily resolvable by XMM-Newton, only ζ^1 Ret is contained with the fields of view of the XMM-Newton cameras. The star is robustly detected (with ∼7700 net counts) in a 20.9 ks XMM-Newton observation (ID 0404920101). No significant variability is observed in the X-ray light curve of ζ^1 Ret (see Figure 13), and the spectrum is well described by a two-component thermal plasma model (with temperatures of ∼0.1 and ∼0.4 keV; see Figure 14 and Table 6).

A.26. HD 136352

There are no significant discrepancies in the stellar physical parameters reported in the literature for HD 136352. The star hosts three confirmed exoplanets, all of which have masses in the super-Earth/sub-Neptune regime. HD 136352 b, c, and d have $M_p \sin i$ of ∼4.7, ∼11, and ∼8.8 $M_\oplus$, respectively, with orbital periods (distances) of ∼11.6 days (∼0.1 au), ∼28 days (∼0.17 au), and ∼107 days (∼0.43 au), respectively. The inner two planets were found to transit the host star by S. R. Kane et al. (2020b), providing bulk densities for the planets. Subsequent observations by L. Delrez et al. (2021) revealed that the third, outer planet also transits the host star. HD 136352 is marginally detected (∼2.7σ) in a 16.9 ks XMM-Newton observation with a count rate of 0.0041 ± 0.0015 counts s^{-1} with the PN camera and medium filter (Table 9).

A.27. GL 327

There are no significant discrepancies in reported stellar parameters of GL 327 in the literature. The system does not host any currently known or candidate exoplanets. GL 327 was robustly detected with ∼10,500 net counts in a 23.5 ks exposure with XMM-Newton (observation ID 0404920201). Count-rate variability was observed in the X-ray spectrum as shown in Figure 13, so we split the observation into three subexposures and modeled the three spectra independently. In all three subexposures, a single-temperature thermal plasma component was sufficient to describe the observations. During the quiescent period from ∼6–21 ks, the plasma temperature was ∼0.4 keV, which increased to ∼0.5 keV during the descending and flaring periods. The normalization during periods of increased X-ray count rate additionally increased by ∼20%. The spectra of GL 327 are shown in Figure 14 (see also Table 6).

A.28. μ Ara

No significant discrepancies in stellar parameters are present in the literature for μ Ara, although there is some uncertainty about the evolutionary stage; we adopt a spectral type of G3IV/V (M. C. Turnbull 2015). μ Ara hosts four known (giant) exoplanets, all detected via RV measurements. HD 160691 b, c, d, and e have masses of $M_p \sin i \sim 1.7$ M_{Jup}, ∼2.4 M_{Jup}, ∼10.2 $M_\oplus$, and ∼0.5 M_{Jup}, respectively, and the planets have orbital periods (orbital distances) of ∼646 days (∼1.5 au), ∼4470 days (∼5.5 au), ∼10 days (∼0.09 au), and ∼307 days (∼0.9 au), respectively. All planetary data were taken from K. Goździewski et al. (2007). μ Ara is not detected in either of the two publicly available XMM-Newton observations.

A.29. κ^1 Cet

There is some discrepancy in the reported age estimates of κ^1 Cet: M. C. Turnbull (2015) listed an age of 2.2 Gyr and G. Takeda et al. (2007) derived an upper limit of <2.76 Gyr, but many studies report significantly younger ages. For example, E. E. Mamajek & L. A. Hillenbrand (2008) derived an age of 300–400 Myr, while M. Güdel et al. (1997) estimated an age of 750 Myr and J. D. Dorren & E. F. Guinan (1994) estimated an age of 650 Myr. There are no currently known or candidate exoplanets orbiting κ^1 Cet.

κ^1 Cet is relatively well-observed in X-rays, with five XMM-Newton observations and two Chandra observations available in the archives, and the star is easily detected in all exposures. It was also observed twice with Chandra using ACIS-S7 in 1/8-subarray mode with a 0.44 s readout time in both observations. While there are clear indications of variability in the light curves of κ^1 Cet, the maximum observed count rate only ever exceeds the median count rate by a factor of ∼2 (see Figure 13). However, despite the only modest changes in count rate, the spectra during these minor flare-like events are quite distinct from the lower count-rate quiescent periods, with significant excess emission at wavelengths shorter than 10 Å compared to quiescent times. The change in count rate is being driven by a significant increase in the temperature (by ∼0.2 keV, or ∼2.3 MK) and normalization (a factor of ∼2.2 increase) of the hottest component in a three-thermal plasma component model (Figure 14; see also Table 6).

A.30. HD 140901

There are no significant discrepancies in the published stellar physical parameters of HD 140901. Two planets have been identified via RV measurements. HD 140901c has $M_p \sin i$ ∼1.8 M_{Jup} with an orbital period of ∼14,390 days (orbital distance of ∼11.8 au; F. Philipot et al. 2023). The existence of HD 140901 b is controversial; if the planet exists, it has a mass of $M_p \sin i$ of ∼16$M_\oplus$ with an orbital period of ∼9 days (orbital distance 0.085 au), but the RV data of HD 140901 can be equally well described by a retrograde orbital inclination of ∼138° (F. Feng et al. 2022; F. Philipot et al. 2023).

HD 140901 was observed once by Chandra/ACIS-I for 24.7 ks. The star was robustly detected with ∼220 net counts. The light curve shows clear evidence for variability (see Figure 13), but the star is not bright enough to enable spectral modeling.

A.31. GJ 777

GJ 777 is a binary star system composed of a G6IV primary (GJ 777A) and an M4.5V secondary (LHS 2509), which are separated by ∼3000 au (∼3′). GJ 777A hosts two currently known exoplanets, detected via RV measurements: HD 190360 b has $M_p \sin i \sim 1.8$ M_{Jup} and an orbital period of ∼2854 days (∼3.9 au; F. Feng et al. 2021), and HD 190360c has $M_p \sin i$ ∼ 19 $M_\oplus$ and an orbital period of ∼17 days (∼0.13 au; L. J. Rosenthal et al. 2021). No X-ray emission is detected coincident with the GJ 777 binary system in either of two snapshot XMM-Newton observations.

A.32. ξ Boo

ξ Boo is a visual binary (ξ Boo A has a spectral type G8V and ξ Boo B has a spectral type K4V; M. C. Turnbull 2015) with an angular separation of ∼4.″9 (orbital period ∼150 yr; R. Wielen 1962); the stars are unresolvable by XMM-Newton (see Figure 12). There are no discrepancies in stellar physical parameters in the literature, and no known or candidate exoplanets. ξ Boo A is a known BY Draconis variable (A. J. Finley et al. 2019).

The ξ Boo binary is robustly detected by XMM-Newton, although the two components cannot be resolved. The system exhibits dramatic X-ray variability, as shown in the light curve in Figure 13. The X-ray spectra of ξ Boo are described by three-component thermal plasma models in all variability states. The flaring spectrum requires hotter temperatures for all three plasma components than the quiescent spectrum, with the normalization of the hottest component increasing by a

factor of ∼3.9 during flaring times compared to quiescent times. Figure 14 shows the best-fit spectral models for ξ Boo (see also Table 6).

A.33. δ Pav

There are no significant discrepancies in the stellar physical parameters reported in the literature for δ Pav. The star does not host any currently known or candidate exoplanets.

δ Pav was detected in a 32.6 ks XMM-Newton observation (ID No. 0780510401) ∼1000 net counts. The A^2 statistic provides evidence that the star may be variable on short timescales; however, there is an insufficient number of counts to split the observation into subexposures (see Figure 13). We attempted to model the spectrum of δ Pav despite the low number of counts; the spectrum required two thermal plasma components to achieve a statistically acceptable fit (see Table 6). The best-fit spectrum in shown in Figure 14.

A.34. LHS 2156

There are no significant discrepancies in the stellar physical parameters reported in the literature for LHS 2156. There are no known or candidate exoplanets in the system.

LHS 2156 was detected with ∼60,000 net counts in a 68.4 ks XMM-Newton observation with the PN camera (thick filter). Figure 13 shows the X-ray light curve, which exhibits count-rate variability over the duration of the observation. The spectra of LHS 2156 are well described by three-component thermal plasma models. The best-fit temperatures and normalizations of two cooler plasma components remain constant within the uncertainties in all subexposures. The hottest thermal plasma component increases in temperature by ∼0.1 keV during flaring periods compared to quiescent periods, an the normalization increases by ∼25%. The best-fit spectra for LHS 2156 are shown in Figure 14 (see also Table 6).

A.35. 82 Eri

There is some discrepancy in the literature about the age of 82 Eri: M. C. Turnbull (2015) and G. Takeda et al. (2007) quoted ages >12 Gyr, but a much younger age of 5.76 ± 0.66 Gyr was found by F. Pepe et al. (2011). 82 Eri hosts four confirmed exoplanets, all of which were discovered via RV measurements (F. Pepe et al. 2011). HD 20794 b, c, d, and e have $M_p \sin i$ values of ∼2.8, ∼2.5, ∼3.5, and ∼4.8 $M_\oplus$, respectively, with orbital periods (distances) of ∼18 days (∼0.13 au), ∼43 days (∼0.23 au), ∼89 days (∼0.26 au), and ∼147 days (∼0.5 au), respectively. All planetary parameters were taken from F. Feng et al. (2017a). 82 Eri has been observed by both XMM-Newton and Chandra (see Table 3), but was not detected in either observation.

A.36. τ Ceti

There are no significant discrepancies in the stellar physical parameters of τ Ceti reported in the literature. τ Ceti hosts four exoplanets, all confirmed via RV measurements (F. Feng et al. 2017b), with some evidence of additional planets in or near the τ Cet HZ (J. Dietrich & D. Apai 2021). τ Ceti e and f both have masses $M_p \sin i$ ∼3.9 $M_\oplus$ with orbital periods of ∼163 days (∼0.55 au) and ∼636 days (∼1.3 au), respectively, while τ Ceti g and h both have masses of $M_p \sin i$ ∼1.8 $M_\oplus$ and orbital periods of ∼20 days (∼0.13 au) and ∼49 days (∼0.24 au), respectively.

τ Ceti was observed by Chandra ACIS-S for 45.1 ks in 1/8-subarray mode and detected at ∼7σ significance with ∼110 net counts. We extracted a light curve from this observation and found an A^2 statistic that is strongly suggestive of variability (see Table 4 and Figure 13), but due to the relatively low number of counts, we did not attempt to extract a spectrum. τ Ceti was marginally detected in an 11.9 ks XMM-Newton observation, but with insufficient counts for light-curve extraction or spectral modeling to be performed. The luminosity estimates for τ Ceti suggest that the star's X-ray luminosity changes by a factor of ∼2.

A.37. 55 Cnc

55 Cnc is a binary star system containing a G8V star (55 Cnc A) and an M4.5V dwarf (55 Cnc B). There are no significant discrepancies in stellar physical parameters. The two components are separated by ∼1065 au (∼1.″4 D. Raghavan et al. 2006). Five exoplanets are known to orbit 55 Cnc A. 55 Cnc b was the first to be discovered (R. P. Butler et al. 1997) with a mass of $M_p \sin i \sim 0.8\ M_{Jup}$ and an orbital period ∼14.7 days (corresponding to an orbital distance of ∼0.11 au; B. E. Nelson et al. 2014; V. Bourrier et al. 2018). 55 Cnc c, d, e, and f have masses of $M_p \sin i \sim 0.16\ M_{Jup}$, ∼3.9 M_{Jup}, ∼8 $M_\oplus$, and ∼0.15 M_{Jup}, respectively, with orbital periods of ∼44 days (∼0.24 au), ∼4870 days (∼5.5 au), ∼0.7 days (∼0.02 au), and ∼260 days (∼0.8 au), respectively.

Cnc 55 was observed twice by Chandra/ACIS-S in 1/8-subarray mode (for 10.7 and 18 ks) and once for 10.4 ks by XMM-Newton. 55 Cnc A was not detected by Chandra, but was detected (at ∼5.6σ significance) by XMM-Newton. No evidence for strong variability was observed in the XMM-Newton light curve of 55 Cnc A (Table 4; see also Figure 13). Despite the relatively low number of net counts, we attempted to model the X-ray spectrum of 55 Cnc A. We find that a single-component thermal plasma model is sufficient to describe the X-ray spectrum (see Table 6 and Figure 14). 55 Cnc B was not detected in the XMM-Newton observation or one of the Chandra observations (the star was not within the field of view of the second Chandra observation).

A.38. 70 Oph

70 Oph is a visual and spectroscopic binary containing a K0V (70 Oph A) star and a K5V (70 Oph B) star with an orbital period of ∼88 yr (D. Pourbaix 2000). The orbit is highly elliptical, with an eccentricity $e = 0.50$ that causes the orbital separation of the stars to vary from ∼11.4 to ∼34.8 au (P. Eggenberger et al. 2008). These orbital separations correspond to angular separations of ∼2.″3–6.″8, unresolvable by XMM-Newton but potentially spatially resolvable by Chandra (see Section 3). P. Eggenberger et al. (2008) found a best-fit age of 6.2 ± 1.0 Gyr, in broad agreement with the 6.8–7.0 Gyr found by Y. K. Tang et al. (2008). These ages (which where derived using asteroseismic observations) are in contrast to the significantly younger age (∼680 Myr) predicted by E. E. Mamajek & L. A. Hillenbrand (2008). There are no currently known or candidate exoplanets in the system.

There are three XMM-Newton observations available for the 70 Oph system. The individual stars are not resolvable in the XMM-Newton observations (see Figure 12); we therefore

cannot separate the X-ray emission from the K0V star (70 Oph A) from the K5V star (70 Oph B) with the currently available observations.

Despite the changes in X-ray count rate observed in the light curves (see Figure 13), the best-fit spectral models of 70 Oph across different VarFlags are nearly indistinguishable (Figure 14; see also Table 6), and the X-ray luminosity of the two stars changes only by ∼40% between the flaring and quiescent periods. Since we cannot separate the X-ray emission of the binary components individually, we do not use the best-fit spectrum of the 70 Oph system as a template for inferring luminosities of other stars in our sample.

A.39. 40 Eri

The 40 Eri triple system contains a K0V star (40 Eri A) that is either in a wide orbit or comoving with a white dwarf (40 Eri B)–M4.5V dwarf (40 Eri C) pair. The projected angular distance between 40 Eri A and 40 Eri BC is ∼1.′3. While the orbital period of the wider A-BC pair is very long, the orbital period of the B–C pair is measured to be ∼230 yr (H. E. Bond et al. 2017; B. D. Mason et al. 2017). The angular separation between 40 Eri B and 40 Eri C is ∼6.″9 , easily resolvable by Chandra (see Figure 2). 40 Eri C has a visual magnitude of ∼11, which we use to estimate $L_{\rm bol}$, and H. M. Johnson & C. D. Wright (1983) estimated $T_{\rm eff}$ to be ∼3100 K. There is one confirmed planet orbiting 40 Eri A, which was discovered via RV measurements. HD 26965 b has $M_{\rm p} \sin i$ of ∼8.5 $M_{\oplus}$ with an orbital period of ∼42 days (B. Ma et al. 2018). No currently known or candidate planets are associated with the 40 Eri BC pair.

The first soft (0.1–2.0 keV) X-ray detection of the 40 Eri system was obtained by HEAO-1, which measured a luminosity of $(9.6 \pm 3.2) \times 10^{28}$ erg s^{-1}(corrected for different distance assumed in that work; W. Cash et al. 1979). Due to the poor spatial resolution of HEAO-1, the binary components could not be resolved. Different scenarios for X-ray production are explored in W. Cash et al. (1979), and the X-ray emission was attributed to 40 Eri C.

The Chandra image of the system clearly shows X-ray sources coincident with both 40 Eri A and C (although not the white dwarf, 40 Eri B; see discussion below). 40 Eri C is the brighter of the two sources, with roughly an order-of-magnitude more net counts than observed for 40 Eri A. There is no evidence for strong variability in either star (see Figure 13). While the coolest thermal plasma component in the 40 Eri C spectrum is similar in temperature to other late-type stars in our sample, the hotter two thermal plasmas are considerably hotter (see Table 6 and Figure 14). Despite the lack of obvious variability in 40 Eri C, the best-fit X-ray spectral parameters most closely resemble those of WX UMa in its flaring and post-flaring states. It is possible this star indeed exhibits significant coronal variability, but it was not detectable in the short snapshot Chandra observation available in the archive.

A.39.1. The White Dwarf 40 Eri B

The white dwarf 40 Eri B is not detected in the 5 ks Chandra/ACIS-S observation of the system. The 3σ upper limit on the count rate is 0.0033 counts s^{-1}. We again use WebPIMMs to convert the observed count rate upper limit to a flux (and luminosity) upper limit, assuming the same spectral model as for WD 1620-391 (Appendix A.19.1). We find a flux upper limit of 1.6×10^{-13} erg s^{-1} cm^{-2}, which corresponds to a luminosity of $\sim 5 \times 10^{25}$ erg s^{-1}. This luminosity upper limit is below the measured X-ray luminosity of G 29-38 ($\sim 8 \times 10^{25}$ erg s^{-1}; T. Cunningham et al. 2022; S. Estrada-Dorado et al. 2023), strongly suggesting a lack of a cold accretion disk around this white dwarf.

A.40. δ Eri

There are no significant discrepancies in the reported physical parameters for δ Eri, and the star does not host any known or candidate exoplanets. δ Eri was observed once with XMM-Newton (observation observation) for 56.2 ks. There was marginal evidence for significant variability in the X-ray light curve of δ Eri (see Figure 13), but the star was too faint for spectral modeling.

A.41. GL 451A (Groombridge 1830)

There are no significant discrepancies in the stellar physical parameters reported in the literature for GL 451A. The system does not host any currently known or candidate exoplanets. GL 451A was observed once with Chandra/ACIS-S (observation ID 9931) for 32.8 ks in 1/8-subarray mode across ACIS detectors 5–7 with a readout time of 0.54 s. No X-ray source is found coincident with the star's position.

A.42. GL 117

M. C. Turnbull (2015) reported an age of 1.5 Gyr for GL 117 and G. Takeda et al. (2007) derived an upper limit of <1.2 Gyr. These ages are in contrast with the very young age (∼100 Myr) predicted by E. E. Mamajek & L. A. Hillenbrand (2008). There are no currently known or candidate exoplanets orbiting GL 117.

GL 117 is robustly detected in XMM-Newton observation 0203060501, and there are low-level count rate variations observable in the light curve (see Figure 13). The largest of these variations reaches a count rate level that is ∼30% above the median count rate. Given the ample number of X-ray counts recorded by XMM-Newton, we divide the light curve into subexposures but we find no significant differences in the best-fit spectral parameters nor the predicted luminosities (see Figure 14 and Table 6). The bright X-ray luminosity of the star, particularly when compared to other K dwarfs in our sample, is consistent with a young age for GL 117.

A.43. GL 783

GL 783 is a binary system containing a K3V star (A) and an M4.5V star (B; M. C. Turnbull & J. C. Tarter 2003). The two stars were stated to be separated by ∼8″ by C. Allen et al. (2000) but Gaia DR3 positions indicate a separation of ∼2.″6 (Gaia Collaboration et al. 2023), both of which are unresolvable by XMM-Newton but potentially spatially resolvable by Chandra (see Section 3). GL 783B has an apparent visual magnitude of ∼12.5 (C. Allen et al. 2000), which we use to estimate $L_{\rm bol}$. At the time of this writing, there were no published values of $T_{\rm eff}$ for GL 783B. The system does not host any currently known or candidate exoplanets.

There is one XMM-Newton observation available for the GL 783 system, and the individual stars are not resolvable (see Figure 12). They therefore cannot separate the X-ray emission

from the K3V star (GL 783A) from the M4.5V star (GL 783B) with the currently available observations. The A^2 statistic provides evidence that one or both stars may be variable on short timescales (see Figure 13); however, there is an insufficient number of counts to split the observation into subexposures. We attempted to model the spectrum of the GL 783 system despite the low number of counts; the spectrum required three thermal plasma components to achieve a statistically acceptable fit (see Figure 14 and Table 6). The coolest thermal plasma component (∼0.1 keV) is similar to the coolest components of the other FGK stars in our sample, while the temperatures of the hottest (∼1 keV) and intermediate (∼0.3 keV) components more closely resemble components found in the later-K and M dwarfs in our sample.

Since we cannot separate the X-ray emission of the binary components individually, we do not use the best-fit spectrum of the GL 783 system as a template for inferring luminosities of other stars in our sample. Follow-up observations with higher spatial resolution are needed to associate the observed X-ray emission with one or both binary components.

A.44. GL 183

There is some discrepancy in the reported spectral type of GL 183: R. O. Gray et al. (2006) reported a spectral type K3V, while K4III is reported by M. C. Turnbull (2015). We adopt a spectral type K3V. There is additional tension in the age estimates, with a younger age (∼2 Gyr) reported by E. E. Mamajek & L. A. Hillenbrand (2008) and older ages reported by M. C. Turnbull (2015; 5.3 Gyr) and G. Takeda et al. (2007; <5.45 Gyr). There are no currently known or candidate exoplanets orbiting GL 183.

GL 183 was detected in an 18.4 ks XMM-Newton observation (ID No. 0780510301) ∼650 net counts. The A^2 statistic provides evidence that the star may be variable on short timescales (see Figure 13); however, there is an insufficient number of counts to split the observation into subexposures. We attempted to model the spectrum of GL 183 despite the low number of counts and found the spectrum required two thermal plasma components to achieve a statistically acceptable fit (Figure 14; see also Table 6), and the fit parameters were reasonably well constrained.

A.45. GJ 667

The GJ 667 is a triple star system wherein the two more-massive components, A and B (both of which are early/mid K dwarfs), orbit one another in a highly elliptical orbit ($e \approx 0.58$). The average angular separation of the two stars is ∼1.″8, possibly resolvable by Chandra. The third star in the system, the M1.5V dwarf GJ 667 C, is separated from the AB pair by ∼0.′5 (which would be easily resolvable with both Chandra and XMM-Newton). There is no published age estimate for the system. GJ 667C has been studied previously in X-rays by A. Brown et al. (2023), and is known to host two confirmed super-Earth exoplanets: GJ 667C b, with $M_p \sin i$ ∼5.6 $M_\oplus$ and an orbital period of ∼7.2 days (∼0.05 au; X. Bonfils et al. 2013; P. Robertson & S. Mahadevan 2014), and GJ 667C c, with $M_p \sin i$ ∼3.8 $M_\oplus$ and an orbital period of ∼28 days (∼0.125 au; G. Anglada-Escudé et al. 2013). An additional three planets in wider orbits were reported by G. Anglada-Escudé et al. (2013) but were unable to be confirmed by P. Robertson & S. Mahadevan (2014); their existence remains controversial.

GJ 667 was observed twice with Chandra/ACIS-S in 1/8-subarray mode. GJ 667 A and B were not within the field of view of either observation. GJ 667 C was detected in both observations. We extracted an X-ray light curve from Chandra ObsID 17317 (with an exposure time of 18.2 ks; see Figure 13), but the star was too faint for spectral modeling to be performed. There were insufficient counts in the second Chandra observation (ObsID 17318, with an exposure time of 9.1 ks) for light-curve or spectral analysis.

A.46. LHS 1875

There is some discrepancy in the literature about the age of LHS 1875: M. C. Turnbull (2015) quoted an age of ∼3.1 Gyr, while G. Takeda et al. (2007) provided a significantly younger upper limit of <0.48 Gyr. There are no known or candidate exoplanets orbiting LHS 1875. LHS 1875 was detected with ∼9260 net counts in a 21.4 ks XMM-Newton/PN observation. No evidence for significant X-ray variability was observed (see Figure 13), and the spectrum was well described by a three-component thermal plasma model (see Table 6).

A.47. GL 570

There is a significant age discrepancy in the literature for the GL 570 quadruple-star system: G. Takeda et al. (2007) reported a very young age of <0.6 Gyr, while M. C. Turnbull (2015) adopted an age of ∼3 Gyr. There are no other significant discrepancies in the stellar physical parameters for the stars in this system. There are no currently known or candidate exoplanets in the system.

GL 570A (K4V) orbits a binary red dwarf pair (GL 570B, an M1.5V dwarf, and GL 570C, an M3V dwarf) with a semimajor axis of ∼190 au (corresponding to an angular separation of ∼0.′5). GL 570A and the GL 570BC pair are both detected in X-rays and are easily resolvable with Chandra (see Figure 12). The red dwarfs that make up the BC pair are separated by ∼0.″2 (J. M. Mariotti et al. 1990; T. Forveille et al. 1999) and cannot be resolved. The fourth component, GL 570D, is a brown dwarf in a very wide orbit (∼4′) from the GL 570 ABC triple system (A. J. Burgasser et al. 2000). GL 570D is not detected in X-rays.

We extract X-ray light curves for both GL 570A and the GL 570BC pair. There is clear evidence for variability in both light curves (see Figure 13), although there are not enough net counts from GL 570BC to enable spectroscopic modeling on subexposures. We therefore divide observation of GL 570A into three distinct subexposures (the first ∼20 ks, 20–30 ks, and 30–40 ks) and independently model the spectra, but only extract one spectrum of GL 570BC from the entire observation. All spectra are well described by a two-component thermal plasma model. The flaring event seen from 20–30 ks in the GL 570A light curve is characterized by changes in plasma temperatures (∼0.1 keV for the cooler component and ∼0.2 keV for the hotter component) and an increase in the hot-component normalization by ∼170%. The different best-fit spectral models for GL 570A, as well as a comparison of the flaring-to-quiescent spectra, are shown in Figure 14. The GL 570A model is overall hotter than the GL 570BC model (see Table 6).

A.48. 61 Cyg

The 61 Cygni AB system is a wide binary containing a K5V star (A) and a K7V star (B), with an angular separation of ∼12″ (the orbital period of the system is ∼659 yr). Most age estimates suggest the system is old (6 ± 1 Gyr; e.g., P. Kervella et al. 2008). The system is resolved by XMM-Newton (J. Robrade et al. 2012). The system does not host any currently known or candidate exoplanets.

61 Cyg has been observed 38 times with XMM-Newton, making it the best X-ray-observed star system in our sample. The observations are spaced ∼6 months apart and span ∼18 yr, and the two stars are well resolved in all available images (see Figure 12). Both stars are observed to flare (see Figure 13), and all of the spectra extracted from both stars are well described by a three-component thermal plasma model. The three best-fit temperatures in the models of 61 Cyg A remain constant within the uncertainties during different variability epochs. The changes in count rate observed during flaring events in 61 Cyg A are driven by changes in the normalizations of the two hotter thermal plasma components (and hence the VEMs): the hottest component normalization increases by an order of magnitude, and the intermediate-temperature component normalization increases by a factor of ∼2.5. The spectra of 61 Cyg B show similar changes in normalization during flaring events, but the two *cooler* plasma components also increase in temperature during flaring events (by ∼0.1 keV). The best-fit spectra for 61 Cyg A and B are shown in Figure 14 (see also Table 6).

A.49. GL 412

The GL 412 AB system contains an M1V primary (A) and a UV Ceti-type flaring M6.6V secondary (B; A. W. Mann et al. 2015, also referred to as WX UMa). X-ray flares were previously observed from the system with ROSAT (J. H. M. M. Schmitt et al. 1995) and attributed to GL 412B; GL 412A was not believed to be a significant source of X-rays. The system does not host any currently known or candidate exoplanets.

The two stars have an angular separation of ∼31″ and are resolved in the XMM-Newton image (observation No. 0742230101; see Figure 2). The image clearly suggests that the observation caught a significant WX UMa flaring event and that the M1V primary, while fainter, emits a detectable quantity of X-ray radiation. A third X-ray source is detected ∼37″ from WX UMa, but is not obviously associated with the GL 412 binary. We measure a count rate of 0.057 ± 0.002 counts s^{-1} in the PN image (medium filter) for GL 412A.

The light curve of GL 412B is shown in Figure 13. Spectral modeling shows that the X-ray luminosity increases by a factor of ∼30 between quiescent and flaring times. The quiescent spectrum (the first ∼2 ks of the observation) is well described with only two thermal plasma components. The steep, ∼0.5 ks flare, the elevated count rate (from ∼3–7 ks), and subsequent declining period all require three components to adequately describe the X-ray spectra. The flaring spectrum exhibits a very hot thermal plasma component, with a temperature of ∼3.5 keV (∼40 MK), which cools as the flare subsides (it has a temperature of ∼2.2 keV during the "elevated" period and ∼1.4 keV during the "descending" count rate period; see Figure 14 and Table 6).

A.50. GJ 832

There are no significant discrepancies in stellar physical parameters, and there is one confirmed exoplanet, GJ 832 b with $M_p \sin i \sim 0.6\ M_{Jup}$ and an orbital period of 3853 days (corresponding to an orbital semimajor axis of ∼3.7 au; J. Bailey et al. 2009; F. Philipot et al. 2023).

GJ 832 was observed twice by XMM-Newton, once during a 8.9 ks (observation 0748010201) exposure during which the star was detected but too faint to enable timing or spectroscopic modeling, and once during a 28.6 ks exposure (observation 0860303301) when the star was overall brighter and underwent a short flaring event (see Figure 13). The quiescent spectrum is well described by two thermal plasma components, while the lower signal-to-noise during the short flaring period allows the flare spectrum to be modeled with a single thermal plasma component. Overall, the luminosity of GJ 832 increases by a factor of ∼2.5 during the flare. The best-fit spectral models and a comparison of the flaring-to-quiescent spectrum are shown in Figure 14 (see also Table 6). The spectrum extracted during the short flaring time during the observation shows an excess of X-ray flux at ∼2–30 Å, but shows weaker X-ray emission (compared to the quiescent spectrum) at wavelengths $\lesssim$2 Å.

A.51. Kapteyn's Star

There are no significant discrepancies in the stellar physical parameters reported in the literature for Kapteyn's Star. Although the detection of a sub-Neptune-mass planet was reported by G. Anglada-Escude et al. (2014), this was later refuted by A. Bortle et al. (2021), who argued that the observed RV variations were artifacts of stellar activity and rotation. There are not currently any additional candidate exoplanets around Kapteyn's Star.

Kapteyn's Star has been observed numerous times by XMM-Newton, Chandra, and Swift (see Table 3), but is not detected in any of archival X-ray observations. We explored whether Kapteyn's Star would be detected in a stacked Chandra X-ray image (the Chandra background is lower and significantly less affected by spurious flaring events than XMM-Newton). The stacked Chandra image has an effective exposure time of 72.5 ks. Kapteyn's Star is still not detected in the stacked image, with a count rate upper limit of $<1.24 \times 10^{-4}$ counts s^{-1}. Assuming the best-fit quiescent spectrum of Wolf 1055, this count rate corresponds to a luminosity upper limit of $<1.1 \times 10^{24}$ erg s^{-1}.

A.52. Wolf 1055

There are no significant discrepancies in the stellar physical parameters of Wolf 1055 or its binary companion VB 10 (GL 572B, an M8V-type BY Draconis flare star; J. Burt et al. 2021). There is one confirmed exoplanet orbiting Wolf 1055: HD 180617 b (also identified as GL 572 Ab), with $M_p \sin i \sim 12\ M_\oplus$ and an orbital period of ∼106 days (∼0.34 au).

Wolf 1055 and VB 10 are separated by ∼1.″2 and are easily resolvable with both XMM-Newton and Chandra. Both Wolf 1055 was observed once with XMM-Newton (for 24.2 ks) and twice with Chandra (with exposure times of 12.2 ks and 29.2 ks). Both Wolf 1055 and VB 10 are detected in all three observations. A comparison of the XMM-Newton observation and the longer Chandra observation (ObsID 7428) is shown in Figure 12. Wolf 1055 is bright enough in two out of these three

observations to enable spectral modeling. However, VB 10 is bright enough to be significantly detected in all three observations, and we are able to extract light curves from all three observations. The light curves of both stars obtained during XMM-Newton observation 0504010101 are shown in Figure 13.

The quiescent spectrum of Wolf 1055 is well described by a three-component thermal plasma model, while the lower signal-to-noise during the flaring period in the second half of the XMM-Newton observation 0504010101 allows the flare spectrum to be modeled with a single thermal plasma component. Overall, the luminosity of Wolf 1055 increases by ∼80% during the flare. The best-fit spectral models and a comparison of the flaring-to-quiescent spectrum are shown in Figure 14 (see also Table 6). The spectrum extracted during the flaring period during the second half of observation shows an excess of X-ray flux at ∼2 Å, and shows weaker X-ray emission (compared to the quiescent spectrum) at wavelengths $\lesssim$2 Å.

A.53. AD Leo

There are no significant discrepancies in the stellar physical parameters reported for AD Leo; all stellar parameters are taken from D. Kossakowski et al. (2022) and references therein. There are no confirmed or candidate exoplanets orbiting AD Leo.

AD Leo is a known flaring star, and exhibits strong X-ray flaring both times the star was observed by XMM-Newton. Both light curves are shown in Figure 13. High count rates enable spectroscopic modeling over multiple subexposures. The X-ray spectra during quiescent periods are generally well described with a two-component thermal plasma model, while periods of flaring and enhanced variability require three thermal plasma components to adequately describe the observed spectra. Increases in X-ray count rate are driven almost entirely by the appearance of this third, hot (∼1.5 keV) thermal plasma component, which drives a significant increase (by 3–5 orders of magnitude) in X-ray emission below ∼2 Å (see Figure 14).

A.54. Wolf 1061

There are no significant discrepancies in stellar physical parameters of Wolf 1061. No age estimate is available for the star. Wolf 1061 hosts three currently known exoplanets (D. J. Wright et al. 2016): Wolf 1061 b, c, and d have masses of $M_p \sin i \sim 1.9$, ∼3.4, and ∼7.7 $M_\oplus$, respectively, with orbital periods of ∼4.9 days (∼0.04 au), ∼17.9 days (∼0.09 au), and ∼217 days (∼0.47 au), respectively. All planetary data taken from N. Astudillo-Defru et al. (2017).

Wolf 1061 was detected in one 38.3 ks observation with Chandra/ACIS-S with ∼240 net counts. The light curve shows evidence for variability (see Figure 13), but the star is not bright enough to enable spectroscopic modeling.

A.55. Luyten's Star

There are no significant discrepancies in the reported stellar parameters for Luyten's Star in the literature. No age estimate is available. There are two confirmed exoplanets orbiting Luyten's Star: GJ 273b and GJ 273 c, which were detected via RV measurements by N. Astudillo-Defru et al. (2017). GJ 273b and GJ 273 c have masses of ∼2.9 and ∼1.2 $M_\oplus$, respectively, and the planets have orbital periods of ∼18.6 days (∼0.09 au) and ∼4.7 days (∼0.03 au), respectively.

Luyten's star is detected at ∼5σ significance in a 28.4 ks observation with Chandra/ACIS-S. The light curve shows evidence of X-ray variability (see Figure 13), but is unable to extract X-ray spectra due to the low number of net counts.

A.56. Proxima Centauri

Proxima Centauri is a member of an extensively studied triple system along with α Cen A and α Cen B. There is currently one confirmed Earthlike exoplanet, Proxima Centauri b, which has $M_p \sin i \sim 1\ M_\oplus$ and an orbital period of ∼11 days (orbital distance ∼0.05 au; G. Anglada-Escudé et al. 2016; M. Damasso et al. 2020; J. P. Faria et al. 2022). Two candidate exoplanets, Proxima Centauri c and d, are awaiting follow-up observations. If present, Prox Cen c (M. Damasso et al. 2020) and d (J. P. Faria et al. 2022) are estimated to have $M_p \sin i$ values of ∼6 $M_\oplus$ and ∼0.26 $M_\oplus$, respectively, with orbital periods (distances) of ∼1900 days (∼1.5 au) and ∼5 days (∼0.029 au).

Proxima Centauri exhibits significant flaring events, such as those illustrated in Figure 3 (see also Figure 13). The X-ray spectrum of Prox Cen is well described by a two-component thermal plasma model (with temperatures of ∼0.25 keV and ∼0.85 keV) during quiescent times and periods of elevated or rising count rates. A third thermal plasma component is required to describe the spectra during flaring periods and during periods of descending count rates following a flare. During the flare, this third component is hot (∼1.5 keV), and cools to ∼0.6 keV as the count rate decreases (see Figure 14 and Table 6). The flaring spectrum drives dramatic increases in both X-ray luminosity. Although the flaring spectrum of Prox Cen exhibits a significant increase in the X-ray flux at wavelengths <10 Å, the spectrum remains elevated (by an order of magnitude) compared to the quiescent spectrum out to long wavelengths (see Figure 7). This is in contrast to earlier-type stars, which generally show a similar X-ray emission between quiescent and flaring periods at wavelengths >100 Å.

Appendix B
Updated X-Ray Luminosities for Swift/XRT-Imaged Stars

We searched the Swift/XRT archive for all nearby stars that did not have available XMM-Newton or Chandra imaging. Nineteen of these stars (mostly K and M dwarfs; one system, Struve 2398, is a binary that is unresolved in the Swift imaging) have fluxes or flux upper limits available from Swift, which we summarize in Table 10. The R.A. and decl. coordinates for each star are taken from Gaia Collaboration et al. (2023), and the stellar physical parameters are from K. G. Stassun et al. (2019). We use the quiescent spectrum from Table 6 of the star that mostly closely matches each Swift star's stellar physical parameters and the Swift response files[18] to convert Swift 0.3–10 keV count rates to luminosities. Figure 15 shows the L_X/L_{bol} ratio as a function of T_{eff} (as in Figure 10) with the 19 Swift stars added.

[18] See https://swift.gsfc.nasa.gov/proposals/swift_responses.html.

Table 10
Stars with Available Swift/XRT Imaging

Star Name	Alternate Name(s)	R.A. (J2000)	Decl. (J2000)	Spectral Type	Distance (pc)	Mass ($M_\odot$)	$T_{\rm eff}$ (K)	$L_{\rm bol}$ ($L_\odot$)	log$L_{\rm X}$ (erg s^{-1})
71 Ori	HIP 29650	06:14:50.77	+19:09:20.29	F6V	20.87	1.35	6533	2.94	<27.59
γ Lep A	GL 216A	05:44:27.45	−22:27:00.08	F6.5V	8.88	1.22	6258	2.34	27.53
ϕ^2 Cet	GL 37	00:50:07.34	−10:38:43.26	F7V	15.77	1.17	6250	1.85	<26.94
η CrB	GL 584A	15:23:12.23	+30:17:17.7	G2V	18.82	1.14	6029	1.64	<27.75
61 Vir	GL 506	13:18:24.97	−18:18:31.0	G7V	8.50	0.91	5585	0.84	<26.78
GL 567	LHS 5279	14:53:23.27	+19:09:13.54	K0V	11.54	0.93	5258	0.54	28.28
GL 68	LHS 1287	01:42:29.41	+20:15:55.87	K1V	7.60	0.88	5190	0.45	<26.29
μ Cas	GL 53A	01:08:22.74	+54:54:47.53	K1V	7.55	0.82	5316	0.46	<26.77
GL 785	LHS 488	20:15:18.88	−27:02:01.61	K2V	8.79	0.85	5071	0.4	<26.50
AK Lep	GL 216B	05:44:26.19	−22:25:24.26	K2V	8.89	0.80	4869	0.3	28.00
GL 688	HD 160346	17:39:16.72	+03:33:17.32	K2V	10.71	0.76	4982	0.34	<26.47
Lacaille 8760	AX Mic	21:17:10.80	−38:52:20.84	K9V	3.97	0.56	3599	0.1	26.89
Wolf 1453	GL 205	05:31:28.21	−03:41:11.50	M1V	5.70	0.56	3690	0.07	27.53
Lacaille 9352	GL 887	23:06:00.94	−35:50:49.79	M1V	3.29	0.54	3676	0.04	26.71
BR Pis	GL 908	23:49:13.59	+02:23:48.90	M1V	5.90	0.41	3685	0.029	<26.80
GL 229A[b]	LHS 1827	06:10:34.46	−21:52:04.16	M1.5V	5.76	0.54	3912	0.06	27.55
GL 1	HD 225213	00:05:31.99	−37:22:03.88	M1.5	4.36	0.38	3696	0.02	26.75
Kruger 60 A	GJ 860A	22:27:58.11	+57:41:38.52	M3V	4.01	0.34	3344	0.01	27.45
Struve 2398B[a]	GL 725B	18:42:43.94	+59:38:18.09	M3V	3.52	0.25	3345	0.021	27.57
Struve 2398A[a]	GL 725A	18:42:43.94	+59:38:06.52	M3.5V	3.52	0.33	3401	0.015	27.57

Notes.
[a] Unresolved binary.
[b] Unresolved binary with a T7 brown dwarf.
(This table is available in machine-readable form in the online article.)

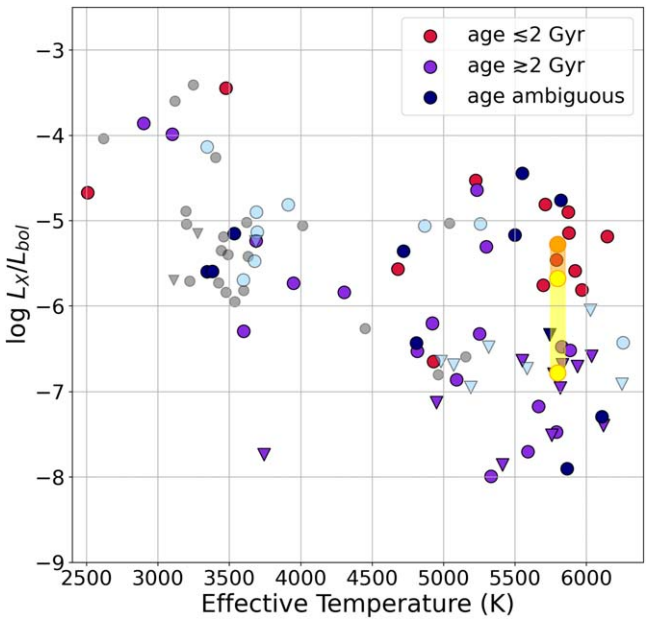

Figure 15. Same as Figure 10 with Swift/XRT sample in light blue.

ORCID iDs

Breanna A. Binder https://orcid.org/0000-0002-4955-0471
Sarah Peacock https://orcid.org/0000-0002-1046-025X
Edward W. Schwieterman https://orcid.org/0000-0002-2949-2163
Margaret C. Turnbull https://orcid.org/0000-0002-0569-1643
Stephen R. Kane https://orcid.org/0000-0002-7084-0529
Alison Farrish https://orcid.org/0000-0003-0944-2334
Katherine Garcia-Sage https://orcid.org/0000-0001-6398-8755

References

Akeson, R., Beichman, C., Kervella, P., Fomalont, E., & Benedict, G. F. 2021, AJ, 162, 14
Allen, C., Poveda, A., & Herrera, M. A. 2000, A&A, 356, 529
Alonso-Floriano, F. J., Morales, J. C., Caballero, J. A., et al. 2015, A&A, 577, A128
Anglada-Escudé, G., Amado, P. J., Barnes, J., et al. 2016, Natur, 536, 437
Anglada-Escude, G., Arriagada, P., Tuomi, M., et al. 2014, MNRAS, 443, L89
Anglada-Escudé, G., Tuomi, M., Gerlach, E., et al. 2013, A&A, 556, A126
Arnaud, K. A. 1996, in ASP Conf. Ser. 101, Astronomical Data Analysis Software and Systems V, ed. G. H. Jacoby & J. Barnes (San Francisco, CA: ASP), 17
Astropy Collaboration, Price-Whelan, A. M., Lim, P. L., et al. 2022, ApJ, 935, 167
Astropy Collaboration, Price-Whelan, A. M., Sipőcz, B. M., et al. 2018, AJ, 156, 123
Astropy Collaboration, Robitaille, T. P., Tollerud, E. J., et al. 2013, A&A, 558, A33
Astudillo-Defru, N., Forveille, T., Bonfils, X., et al. 2017, A&A, 602, A88
Ayres, T. 2023, AJ, 166, 212
Bailey, J., Butler, R. P., Tinney, C. G., et al. 2009, ApJ, 690, 743
Baraffe, I., Homeier, D., Allard, F., & Chabrier, G. 2015, A&A, 577, A42
Benedict, G. F., McArthur, B. E., Nelan, E. P., et al. 2022, AJ, 163, 295
Betremieux, Y., & Kaltenegger, L. 2013, ApJ, 772, L31
Betremieux, Y., & Kaltenegger, L. 2014, ApJ, 791, 7
Bidelman, W. P. 1985, ApJS, 59, 197
Bond, H. E., Bergeron, P., & Bédard, A. 2017, ApJ, 848, 16
Bonfils, X., Delfosse, X., Udry, S., et al. 2013, A&A, 549, A109
Bortle, A., Fausey, H., Ji, J., et al. 2021, AJ, 161, 230
Bourrier, V., Dumusque, X., Dorn, C., et al. 2018, A&A, 619, A1
Brandl, B. R., Absil, O., Agócs, T., et al. 2018, Proc. SPIE, 10702, 107021U
Brewer, J. M., Zhao, L. L., Fischer, D. A., et al. 2023, AJ, 166, 46
Brown, A., Schneider, P. C., France, K., et al. 2023, AJ, 165, 195
Bryson, S., Kunimoto, M., Kopparapu, R. K., et al. 2021, AJ, 161, 36
Burgasser, A. J., Kirkpatrick, J. D., Cutri, R. M., et al. 2000, ApJL, 531, L57
Burke, C. J., Christiansen, J. L., Mullally, F., et al. 2015, ApJ, 809, 8
Burt, J., Feng, F., Holden, B., et al. 2021, AJ, 161, 10
Butler, R. P., Marcy, G. W., Williams, E., Hauser, H., & Shirts, P. 1997, ApJL, 474, L115

Casagrande, L., Flynn, C., & Bessell, M. 2008, MNRAS, 389, 585
Cash, W., Charles, P., Bowyer, S., et al. 1979, ApJL, 231, L137
Crass, J., Gaudi, B. S., Leifer, S., et al. 2021, arXiv:2107.14291
Cunningham, T., Wheatley, P. J., Tremblay, P.-E., et al. 2022, Natur, 602, 219
Currie, T., Biller, B., Lagrange, A., et al. 2023, in ASP Conf. Ser. 534, Protostars and Planets VII, ed. S. Inutsuka et al. (San Francisco, CA: ASP), 799
Damasso, M., Del Sordo, F., Anglada-Escudé, G., et al. 2020, SciA, 6, eaax7467
Dattilo, A., Batalha, N. M., & Bryson, S. 2023, AJ, 166, 122
del Peloso, E. F., da Silva, L., & Porto de Mello, G. F. 2000, A&A, 358, 233
Delrez, L., Ehrenreich, D., Alibert, Y., et al. 2021, NatAs, 5, 775
Dietrich, J., & Apai, D. 2021, AJ, 161, 17
do Amaral, L. N. R., Barnes, R., Segura, A., & Luger, R. 2022, ApJ, 928, 12
Dorren, J. D., & Guinan, E. F. 1994, ApJ, 428, 805
Dumusque, X., Pepe, F., Lovis, C., et al. 2012, Natur, 491, 207
Eggenberger, P., Miglio, A., Carrier, F., Fernandes, J., & Santos, N. C. 2008, A&A, 482, 631
Estrada-Dorado, S., Guerrero, M. A., Toalá, J. A., et al. 2023, ApJL, 944, L46
Faria, J. P., Suárez Mascareño, A., Figueira, P., et al. 2022, A&A, 658, A115
Feigelson, E. D., Kashyap, V. L., & Siemiginowska, A. 2022, in Handbook of X-ray and Gamma-ray Astrophysics, ed. C. Bambi & A. Santangelo (Singapore: Springer), 119
Feng, F., Anglada-Escude, G., Tuomi, M., et al. 2019, MNRAS, 490, 5002
Feng, F., Butler, R. P., Jones, H. R. A., et al. 2021, MNRAS, 507, 2856
Feng, F., Butler, R. P., Vogt, S. S., et al. 2022, ApJS, 262, 21
Feng, F., Tuomi, M., & Jones, H. R. A. 2017a, A&A, 605, A103
Feng, F., Tuomi, M., Jones, H. R. A., et al. 2017b, AJ, 154, 135
Fernandes, J., Lebreton, Y., Baglin, A., & Morel, P. 1998, A&A, 338, 455
Finley, A. J., See, V., & Matt, S. P. 2019, ApJ, 876, 44
Forveille, T., Beuzit, J.-L., Delfosse, X., et al. 1999, A&A, 351, 619
France, K., Duvvuri, G., Egan, H., et al. 2020, AJ, 160, 237
France, K., Loyd, R. O. P., Youngblood, A., et al. 2016, ApJ, 820, 89
Fromont, E. F., Ahlers, J. P., do Amaral, L. N. R., et al. 2024, ApJ, 961, 115
Fruscione, A., McDowell, J. C., Allen, G. E., et al. 2006, Proc. SPIE, 6270, 62701V
Fujii, Y., Angerhausen, D., Deitrick, R., et al. 2018, AsBio, 18, 739
Fulton, B. J., Petigura, E. A., Howard, A. W., et al. 2017, AJ, 154, 109
Gaia Collaboration 2021, A&A, 649, 1
Gaia Collaboration, Vallenari, A., Brown, A. G. A., et al. 2023, A&A, 674, A1
Gandolfi, D., Barragán, O., Livingston, J. H., et al. 2018, A&A, 619, L10
García Muñoz, A., Zapatero Osorio, M. R., Barrena, R., et al. 2012, ApJ, 755, 103
Garcia-Sage, K., Glocer, A., Drake, J. J., Gronoff, G., & Cohen, O. 2017, ApJL, 844, L13
Gaudi, B. S., Seager, S., Mennesson, B., et al. 2020, arXiv:2001.06683
Ghezzi, L., Cunha, K., Smith, V. V., et al. 2010, ApJ, 720, 1290
Gillon, M., Demory, B.-O., Van Grootel, V., et al. 2017, NatAs, 1, 0056
Goździewski, K., Maciejewski, A. J., & Migaszewski, C. 2007, ApJ, 657, 546
Grant, C. E., Bautz, M. W., Plucinsky, P. P., & Ford, P. G. 2024, arXiv:2406.18395
Gray, R. O., Corbally, C. J., Garrison, R. F., et al. 2006, AJ, 132, 161
Gray, R. O., Corbally, C. J., Garrison, R. F., McFadden, M. T., & Robinson, P. E. 2003, AJ, 126, 2048
Greene, T. P., Bell, T. J., Ducrot, E., et al. 2023, Natur, 618, 39
Güdel, M., Guinan, E. F., & Skinner, S. L. 1997, ApJ, 483, 947
Han, I., & Gatewood, G. 2002, PASP, 114, 224
Harada, C. K., Dressing, C. D., Kane, S. R., & Ardestani, B. A. 2024, ApJS, 272, 30
Hatzes, A. P., Gandolfi, D., Korth, J., et al. 2022, AJ, 163, 223
Hawley, S. L., Gizis, J. E., & Reid, I. N. 1996, AJ, 112, 2799
Hinkel, N. R., & Unterborn, C. T. 2018, ApJ, 853, 83
Holberg, J. B., Oswalt, T. D., & Sion, E. M. 2002, ApJ, 571, 512
Holberg, J. B., Oswalt, T. D., Sion, E. M., Barstow, M. A., & Burleigh, M. R. 2013, MNRAS, 435, 2077
Holmberg, J., Nordström, B., & Andersen, J. 2009, A&A, 501, 941
Huang, C. X., Burt, J., Vanderburg, A., et al. 2018, ApJL, 868, L39
Johnson, H. M., & Wright, C. D. 1983, ApJS, 53, 643
Johnstone, C. P., Bartel, M., & Güdel, M. 2021, A&A, 649, A96
Jones, H. R. A., Paul Butler, R., Tinney, C. G., et al. 2002, MNRAS, 333, 871
Kane, S. R. 2023, ApJ, 958, 120
Kane, S. R., Kopparapu, R. K., & Domagal-Goldman, S. D. 2014, ApJL, 794, L5
Kane, S. R., Meshkat, T., & Turnbull, M. C. 2018, AJ, 156, 267
Kane, S. R., Roettenbacher, R. M., Unterborn, C. T., Foley, B. J., & Hill, M. L. 2020a, PSJ, 1, 36
Kane, S. R., Yalçınkaya, S., Osborn, H. P., et al. 2020b, AJ, 160, 129
Kervella, P., Thévenin, F., Ségransan, D., et al. 2003, A&A, 404, 1087
Kervella, P., Mérand, A., Pichon, B., et al. 2008, A&A, 488, 667
Kite, E. S., & Barnett, M. N. 2020, PNAS, 117, 18264
Kopparapu, R. K., Hébrard, E., Belikov, R., et al. 2018, ApJ, 856, 122
Kossakowski, D., Kürster, M., Henning, T., et al. 2022, A&A, 666, A143
Krissansen-Totton, J., & Fortney, J. J. 2022, ApJ, 933, 115
Kunimoto, M., & Matthews, J. M. 2020, AJ, 159, 248
Kürster, M., Endl, M., Els, S., et al. 2000, A&A, 353, L33
Laliotis, K., Burt, J. A., Mamajek, E. E., et al. 2023, AJ, 165, 176
Latković, O., Čeki, A., & Lazarević, S. 2021, ApJS, 254, 10
Li, Z., Hildebrandt, S. R., Kane, S. R., et al. 2021, AJ, 162, 9
Lincowski, A. P., Meadows, V. S., Zieba, S., et al. 2023, ApJL, 955, L7
Linsky, J. L., & Redfield, S. 2024, SSRv, 220, 32
Linsky, J. L., Wood, B. E., Youngblood, A., et al. 2020, ApJ, 902, 3
Louca, A. J., Miguel, Y., Tsai, S.-M., et al. 2023, MNRAS, 521, 3333
Loyd, R. O. P., France, K., Youngblood, A., et al. 2018b, ApJ, 867, 71
Loyd, R. O. P., Shkolnik, E. L., Schneider, A. C., et al. 2018a, ApJ, 867, 70
Lu, W., Rucinski, S. M., & Ogłoza, W. 2001, AJ, 122, 402
Luger, R., & Barnes, R. 2015, AsBio, 15, 119
Lustig-Yaeger, J., Meadows, V. S., & Lincowski, A. P. 2019, AJ, 158, 27
Lustig-Yaeger, J., Fu, G., May, E. M., et al. 2023, NatAs, 7, 1317
Ma, B., Ge, J., Muterspaugh, M., et al. 2018, MNRAS, 480, 2411
Mamajek, E., & Stapelfeldt, K. 2024, arXiv:2402.12414
Mamajek, E. E., & Hillenbrand, L. A. 2008, ApJ, 687, 1264
Mann, A. W., Feiden, G. A., Gaidos, E., Boyajian, T., & von Braun, K. 2015, ApJ, 804, 64
Mariotti, J. M., Perrier, C., Duquennoy, A., & Duhoux, P. 1990, A&A, 230, 77
Marounina, N., & Rogers, L. A. 2020, ApJ, 890, 107
Mason, B. D., Hartkopf, W. I., & Miles, K. N. 2017, AJ, 154, 200
Mayor, M., & Queloz, D. 1995, Natur, 378, 355
Mayor, M., Udry, S., Naef, D., et al. 2004, A&A, 415, 391
Meadows, V. S., Lincowski, A. P., & Lustig-Yaeger, J. 2023, PSJ, 4, 192
Moran, S. E., Stevenson, K. B., Sing, D. K., et al. 2023, ApJL, 948, L11
Morgan, R., Savransky, D., Turmon, M., et al. 2021, JATIS, 7, 021220
Mosser, B., Deheuvels, S., Michel, E., et al. 2008, A&A, 488, 635
Mugrauer, M. 2019, MNRAS, 490, 5088
National Academies of Sciences, Engineering, and Medicine 2023, Pathways to Discovery in Astronomy and Astrophysics for the 2020s (Washington, DC: The National Academies Press)
Nelson, B. E., Ford, E. B., Wright, J. T., et al. 2014, MNRAS, 441, 442
Nordström, B., Mayor, M., Andersen, J., et al. 2004, A&A, 418, 989
Obridko, V. N., Ragulskaya, M. V., & Khramova, E. G. 2020, JASTP, 208, 105395
Pace, G., & Pasquini, L. 2004, A&A, 426, 1021
Peacock, S., Barman, T., Shkolnik, E. L., et al. 2020, ApJ, 895, 5
Pepe, F., Lovis, C., Ségransan, D., et al. 2011, A&A, 534, A58
Philipot, F., Lagrange, A. M., Kiefer, F., et al. 2023, A&A, 678, A107
Pidhorodetska, D., Fauchez, T. J., Villanueva, G. L., Domagal-Goldman, S. D., & Kopparapu, R. K. 2020, ApJL, 898, L33
Pineda, J. S., Youngblood, A., & France, K. 2021, ApJ, 918, 40
Porto de Mello, G. F., & da Silva, L. 1997, ApJL, 476, L89
Pourbaix, D. 2000, A&AS, 145, 215
Pravdo, S. H., & Shaklan, S. B. 2009, ApJ, 700, 623
Quanz, S. P., Crossfield, I., Meyer, M. R., Schmalzl, E., & Held, J. 2015, IJAsB, 14, 279
Raghavan, D., Henry, T. J., Mason, B. D., et al. 2006, ApJ, 646, 523
Rahman, M., & Chakrobartty, S. 2004, J. Korean Data Inform. Sci. Soc., 15, 211, https://koreascience.kr/article/JAKO200423421079798.page
Rajpaul, V., Aigrain, S., & Roberts, S. 2016, MNRAS, 456, L6
Richey-Yowell, T., Shkolnik, E. L., Schneider, A. C., et al. 2019, ApJ, 872, 17
Richey-Yowell, T., Shkolnik, E. L., Schneider, A. C., et al. 2023, ApJ, 951, 44
Robertson, P., & Mahadevan, S. 2014, ApJL, 793, L24
Robrade, J., Schmitt, J. H. M. M., & Favata, F. 2012, A&A, 543, A84
Roettenbacher, R. M., & Kane, S. R. 2017, ApJ, 851, 77
Rosenthal, L. J., Fulton, B. J., Hirsch, L. A., et al. 2021, ApJS, 255, 8
Rugheimer, S., Kaltenegger, L., Segura, A., Linsky, J., & Mohanty, S. 2015, ApJ, 809, 57
Santos, N. C., Sousa, S. G., Mortier, A., et al. 2013, A&A, 556, A150
Sanz-Forcada, J., Micela, G., Ribas, I., et al. 2011, A&A, 532, A6
Sanz-Forcada, J., Ribas, I., Micela, G., et al. 2010, A&A, 511, L8
Sanz-Forcada, J., Stelzer, B., Coffaro, M., Raetz, S., & Alvarado-Gómez, J. D. 2019, A&A, 631, A45
Scargle, J. D. 1998, ApJ, 504, 405
Scargle, J. D., Norris, J. P., Jackson, B., & Chiang, J. 2013, ApJ, 764, 167
Schmitt, J. H. M. M. 1997, A&A, 318, 215

Schmitt, J. H. M. M., Fleming, T. A., & Giampapa, M. S. 1995, ApJ, 450, 392
Schwieterman, E. W., Kiang, N. Y., Parenteau, M. N., et al. 2018, AsBio, 18, 663
Smith, R., Wyatt, M. C., & Dent, W. R. F. 2008, A&A, 485, 897
Stassun, K. G., Collins, K. A., & Gaudi, B. S. 2017, AJ, 153, 136
Stassun, K. G., Oelkers, R. J., Paegert, M., et al. 2019, AJ, 158, 138
Swain, M. R., Estrela, R., Roudier, G. M., et al. 2021, AJ, 161, 213
Takeda, G., Ford, E. B., Sills, A., et al. 2007, ApJS, 168, 297
Tang, Y. K., Bi, S. L., & Gai, N. 2008, NewA, 13, 541
The LUVOIR Team 2019, arXiv:1912.06219
Tokovinin, A. 2012, AJ, 144, 56
Turnbull, M. C. 2015, arXiv:1510.01731
Turnbull, M. C., & Tarter, J. C. 2003, ApJS, 149, 423
Turnbull, M. C., Glassman, T., Roberge, A., et al. 2012, PASP, 124, 418
Turnbull, M. C., Zimmerman, N., Girard, J. H., et al. 2021, JATIS, 7, 021218
Udry, S., Dumusque, X., Lovis, C., et al. 2019, A&A, 622, A37
Unterborn, C. T., Desch, S. J., Haldemann, J., et al. 2023, ApJ, 944, 42
Unterborn, C. T., Foley, B. J., Desch, S. J., et al. 2022, ApJL, 930, L6
Van Eylen, V., Lund, M. N., Silva Aguirre, V., et al. 2014, ApJ, 782, 14
Wielen, R. 1962, AJ, 67, 599
Wilms, J., Allen, A., & McCray, R. 2000, ApJ, 542, 914
Wright, D. J., Wittenmyer, R. A., Tinney, C. G., Bentley, J. S., & Zhao, J. 2016, ApJL, 817, L20
Wyatt, M. C., Greaves, J. S., Dent, W. R. F., & Coulson, I. M. 2005, ApJ, 620, 492
Wyatt, M. C., Smith, R., Greaves, J. S., et al. 2007, ApJ, 658, 569
Zasche, P., Wolf, M., Hartkopf, W. I., et al. 2009, AJ, 138, 664
Zhang, J., Zhao, J., Oswalt, T. D., et al. 2019, ApJ, 887, 84
Zieba, S., Kreidberg, L., Ducrot, E., et al. 2023, Natur, 620, 746
Zirm, H. 2011, JDSO, 7, 24